

Astrophysical Journal, in press

Spatially Resolved PAH Emission Features in Nearby, Low Metallicity, Star-Forming Galaxies

Korey Haynes

Department of Physics & Astronomy, Macalester College, 1600 Grand Avenue, Saint Paul, MN 55105

Department of Physics & Astronomy, George Mason University, Fairfax, VA 22030

khaynes5@gmu.edu

John M. Cannon

Department of Physics & Astronomy, Macalester College, 1600 Grand Avenue, Saint Paul, MN 55105

jcannon@macalester.edu

Evan D. Skillman

Department of Astronomy, University of Minnesota, Minneapolis, MN 55455

skillman@astro.umn.edu

Dale C. Jackson

Sandia National Laboratories, Albuquerque, New Mexico

dcjacks@sandia.gov

Robert D. Gehrz

Department of Astronomy, University of Minnesota, Minneapolis, MN 55455

gehrz@astro.umn.edu

ABSTRACT

Low-resolution, mid-infrared *Spitzer*/IRS spectral maps are presented for three nearby, low-metallicity dwarf galaxies (NGC 55, NGC 3109 and IC 5152) for the purpose of examining the spatial distribution and variation of polycyclic aromatic hydrocarbon (PAH) emission. The sample straddles a metallicity of $12 + \log(\text{O}/\text{H}) \approx 8$, a transition point below which PAH intensity empirically drops and the character of the interstellar medium changes. We derive quantitative radiances of PAH features and atomic lines on both global and spatially-resolved scales. The *Spitzer* spectra, combined with extensive ancillary data from the UV through the mid-infrared, allow us to examine changes in the physical environments and in PAH feature radiances down to a physical scale of ~ 50 pc. We discuss correlations between various PAH emission feature and atomic line radiances. The $(6.2 \mu\text{m})/(11.3 \mu\text{m})$, $(7.7 \mu\text{m})/(11.3 \mu\text{m})$, $(8.6 \mu\text{m})/(11.3 \mu\text{m})$, $(7.7 \mu\text{m})/(6.2 \mu\text{m})$, and $(8.6 \mu\text{m})/(6.2 \mu\text{m})$ PAH radiance ratios are found to be independent of position across all three galaxies, although the ratios do vary from galaxy to galaxy. As seen in other galaxies, we find no variation in the grain size distribution as a function of local radiation field strength. Absolute PAH feature intensities as measured by a ratio of PAH/(24 μm) radiances are seen to vary both positionally within a given galaxy, and from one galaxy to another when integrated over the full observed extent of each system. We examine direct comparisons of CC mode PAH ratios $(7.7 \mu\text{m})/(6.2 \mu\text{m})$ and $(8.6 \mu\text{m})/(6.2 \mu\text{m})$ to the mixed (CC/CH) mode PAH ratio $(7.7 \mu\text{m})/(11.3 \mu\text{m})$. We find little variation in either mode, and no difference in trends between modes. While the local conditions change markedly over the observed regions of these galaxies, the properties of PAH emission show a remarkable degree of uniformity.

Subject headings: galaxies: evolution — galaxies: dwarf — galaxies: irregular — galaxies: individual (NGC 55, NGC 3109, IC 5152)

1. Introduction

1.1. On The Origin of PAH Emission Features

The mid-infrared (MIR; $\sim 3\text{--}20 \mu\text{m}$) is a very rich spectral regime. The Rayleigh Jean’s tail of the stellar spectral energy distribution (SED) contributes at short wavelengths, and the rise of the warm dust continuum contributes at long wavelengths. Between them is the large silicate extinction feature centered around $9.7 \mu\text{m}$. Superposed on this complex continuum are numerous broad emission features (notably at $3.3 \mu\text{m}$, $6.2 \mu\text{m}$, $7.7 \mu\text{m}$, 8.6

μm , 11.3 μm and 12.6 μm) and atomic lines (e.g., [S IV] at 10.5 μm , [Ne II] at 12.8 μm , [Ne III] at 15.56 μm , and [S III] at 18.71 μm , among others). The broad emission features are attributed to vibrational transitions from polycyclic aromatic hydrocarbon (PAH) molecules.

PAHs are planar molecules containing tens to thousands of carbon atoms. While the assignment of these features to specific molecules is still an area of very active theoretical and laboratory investigation, it is generally agreed that this type of molecule (carbon atoms arranged in a system of fused hexagonal rings terminated by carbon-hydrogen single bonds) produces the broad emission features in the MIR spectral range. The four most luminous features in astrophysical sources appear at wavelengths of 6.2 μm , 7.7 μm , 8.6 μm and 11.3 μm (Leger & Puget 1984). These emission features are produced following the absorption of energetic (typically far-ultraviolet) photons by PAH molecules; the molecules bend and stretch in fundamental modes that produce infrared photons as this energy is dissipated.

There are two principal types of vibrational modes in PAH molecules. The first involves the stretching of carbon-carbon (CC) bonds and contributes to the features at 6.2 μm , 7.7 μm and 8.6 μm . The second involves the bending of carbon-hydrogen (CH) bonds; these modes can occur either in the plane (“wagging” modes) or out of the plane of the molecule. The wagging mode contributes to the 7.7 μm and 8.6 μm features, while the out-of-plane bending mode is less energetic and contributes to the 11.3 μm feature. For detailed discussions of these mode assignments (some of which are still under investigation) we refer the reader to Allamandola et al. (1989), Draine & Li (2007), Tielens (2008), Bauschlicher et al. (2008, 2009) and the many references therein.

The relative variations in intensity of these features is sensitive to both the physical size and to the ionization state (i.e., to the hardness of the radiation field) of the molecules. It is generally accepted that the smallest PAH molecules produce the shortest-wavelength features, and that increasing the number of carbon atoms leads to increased intensities of the longer wavelength features. However, this simple interpretation is clouded somewhat by the prediction that the 7.7 μm band is produced by a mixture of both small and large molecules (Bauschlicher et al. 2009). Evidence is also mounting that the 6.2 μm feature may arise from PAHs with different compositions than the longer-wavelength features, either from the inclusion of N atoms (Bauschlicher et al. 2008, 2009) or from the carriers being among the simplest C-based ring structures (e.g., protonated naphthalene; Ricks et al. 2009). In this simple model, the ratios of radiances of long-wavelength PAH features to shorter-wavelength features provides a diagnostic of the grain size distribution; examining the changes in the grain size distribution as a function of local conditions is one of the primary goals of this study.

The hardness of the radiation field also contributes to the variations in intensity of the

various PAH bands. Laboratory predictions (e.g., Allamandola et al. 1999; Kim & Saykally 2002; Bauschlicher 2002) suggest that ionized PAH molecules produce stronger CC mode vibrations (e.g., Bakes et al. 2001). Bauschlicher et al. (2008) finds that the intensities of the CC modes arising from cationic PAHs are increased by an order of magnitude or more compared to neutral species. Observationally this manifests itself as a strengthening of the CC modes (i.e., the $6.2\ \mu\text{m}$, $7.7\ \mu\text{m}$ and $8.6\ \mu\text{m}$ PAH features) relative to the CH modes (primarily the $11.3\ \mu\text{m}$ feature, although the $8.6\ \mu\text{m}$ feature is also affected to a lesser extent) in a given source. Quantitative studies have been undertaken to attempt to connect these variations of PAH intensities to the physical conditions of the gas in a variety of astrophysical environments (see further discussion below).

1.2. Studying PAH Emission in Nearby Galaxies

Galaxies radiate a large percentage of their total luminosity in the infrared, from tens of percent in star forming galaxies up to 99% in ultra luminous infrared galaxies (Sanders et al. 1988; Sanders & Mirabel 1996). An especially rich segment of the IR region falls between $\sim 3\ \mu\text{m}$ - $20\ \mu\text{m}$, where emission features from PAHs arise in most star-forming galaxies. The emission from PAHs varies from a few percent up to 20% of the total MIR luminosity in normal galaxies (Helou et al. 2000), but this percentage drops sharply with decreasing metallicity (Engelbracht et al. 2005; Jackson et al. 2006; Smith et al. 2007). Isolating the processes that affect PAH emission intensity allows investigation of the physical conditions present in star forming regions (Kennicutt et al. 2003). This in turn leads to enhanced understanding of the interplay between PAH emission and star formation, the role of radiation field characteristics in governing PAH intensities, and the stellar-interstellar medium connection.

Many investigations have been conducted on PAH emission in a wide range of galaxy types, but the observations of low-metallicity galaxies in particular have been challenging, in large part due to the difficulties of obtaining spectra of sufficient sensitivity and spatial resolution from low-mass (and often low surface-brightness) galaxies. Using Infrared Array Camera (IRAC) imaging, Engelbracht et al. (2005) discovered a threshold metallicity of $12 + \log(\text{O}/\text{H}) \approx 8$, below which PAH intensity drops sharply, and these results have been confirmed by a number of other studies (e.g., Hogg et al. 2005; O’Halloran et al. 2006; Jackson et al. 2006; Rosenberg et al. 2006; Engelbracht et al. 2008; Wu et al. 2010, and references therein). This metallicity apparently signifies a fundamental change in the nature of the interstellar medium (ISM); the molecular component of more metal-rich galaxies is easily studied via CO observations. However, in systems more metal-poor than $\sim 25\% Z_{\odot}$, CO no longer traces H_2 accurately and the dominant molecular component by mass remains largely

unconstrained (Taylor et al. 1998; Leroy et al. 2005). In this regard, PAH observations of metal-poor galaxies are especially important, as they provide one of our only probes of an otherwise elusive ISM component.

Multiple factors have been found to influence the amount of infrared emission from PAH molecules. The metal content of the host galaxy might be expected to play an important role, since the carrier molecules consist in part of heavy elements. Indeed, Rosenberg et al. (2006) find a correlation between diffuse $8\ \mu\text{m}$ luminosity and metallicity for a large sample of star-forming dwarf galaxies. The same investigation also finds a more significant correlation between PAH luminosity and current star formation rate (SFR) than with metallicity. The Gordon et al. (2008) study of H II regions in M 101 reaches a similar conclusion, where PAH luminosities are more closely tied to the local ionization index than to the metallicity. These results suggest that multiple factors contribute to the observed PAH luminosity in a given region, including process related to both the growth and the stimulation of the molecules.

Dwarf galaxies offer canonically “simple” environments in which to explore variations in the intensities of PAH features and emissions. Their characteristically low masses make them more susceptible than spiral galaxies to turbulence and feedback (Tenorio-Tagle & Bodenheimer 1988), allowing recent disturbances of the galaxy’s dust and gas to be readily seen. Typical dwarfs display solid body rotation and lack shear, preserving structures in the ISM. Dwarf galaxies are abundant in the local universe, and were even more so in the past. The low metallicities typical of these systems approximate the conditions of high redshift galaxies, revealing the physical properties of some of the most distant galaxies by using some of the nearest as a proxy.

Previous studies of PAH emission in dwarf galaxies have sought to explain how these molecules form, survive, and are destroyed in low-metallicity systems. Jackson et al. (2006) observed a sample of 15 Local Group dwarfs, including the 3 galaxies in the present study. They find that both metallicity and local radiation field properties influence the intensity of PAH emission. They also find that diffuse $8\ \mu\text{m}$ emission (strictly a nonlinear composite of the $6.2\ \mu\text{m}$, $7.7\ \mu\text{m}$ and $8.6\ \mu\text{m}$ PAH features, as well as the underlying warm dust continuum) cannot be predicted by the mass of the galaxy alone. Another concern was whether younger systems have time to populate their ISM with the requisite metals to grow PAHs in the first place, but Jackson et al. (2006) rules out this hypothesis. The galaxies in their sample (and therefore ours) have all populated their asymptotic giant branch (AGB), and therefore have the necessary metals to grow PAHs (see, for example, the discussion in Tielens 2008), whether or not they display PAH emission. They also dismiss outflow being responsible for removing PAHs from low-mass galaxies since the HI distributions for the galaxies in their sample lack evidence of large-scale blowout. However, the relative importance of PAH

destruction remains an open issue; SNe may be able to destroy PAHs at a rate comparable to the production rate in low-metallicity environments.

Environmental differences in the character of PAH emission have already been observed within galaxies using *Spitzer* data (e.g., Smith et al. 2007; Dale et al. 2009). In spiral systems with large, well-defined structures, this is to be expected. The nuclear regions, spiral arms, inter-arm regions, and extended disks of such galaxies can have vastly different physical conditions, as well as different chemical compositions and SFRs. In contrast, dwarf galaxies present surprisingly uniform metallicity throughout their high surface brightness components (e.g., Kobulnicky & Skillman 1996, 1997). While star formation regions are often scattered throughout the disks of dwarfs, these regions appear to have only a minimal effect on the metallicity of the surrounding interstellar gas.

The uniform metal content within a given dwarf galaxy is particularly relevant to the issue of stimulating PAH carriers into emission. It has been shown that PAH emission highlights the edges of photodissociation regions (PDRs) in spiral galaxies (Giard et al. 1994; Helou et al. 2001, 2004). As a result, it has been proposed that radiation inside PDRs is too intense for the survival of PAH molecules, while at large distances from PDRs the radiation field would be too weak to stimulate the molecules. There is also evidence that in regions of hard and/or strong radiation fields, the type of PAH carrier can have a marked effect on the relative PAH intensities (Compiègne et al. 2007). If radiation field strength were the only factor affecting the emission from PAH carriers, then the uniform metallicity ISM of dwarfs would reveal this as a correspondence between the locations of massive stars and the presence of PAH emission. However, PAH emission has been observed in the quiescent ISM of dwarfs via imaging (e.g., Cannon et al. 2006; Jackson et al. 2006), including in the galaxies observed in this study, so the physical proximity of PAHs to PDRs cannot act alone in governing the amount of emission from PAH molecules in the metal-poor ISM.

The spatially resolved properties of PAH emission using spectra have not been investigated extensively for low-metallicity systems, though many studies of diffuse emission (arising from multiple PAH features within a bandpass) are now in the literature (see above). In this paper, we examine the intensities and spatial variations of several PAH features in three low-metallicity dwarf galaxies. This approach allows one to separate and study the individual PAH bands contained within the comparatively broad IRAC bandpasses. Our interest is in both how the relative intensities of these features change from one galaxy to the next, and more importantly, within a given galaxy. A comparison of the ratios of PAH bands within a galaxy should be instructive as to how environmental factors and PAH intensities are related. As one effort to trace these environmental factors, maps of [Ne II] emission are also extracted from our spectral maps. These images reveal the morphology of ionized gas

and offer insights into how local radiation field properties affect the relative fluxes of the various PAH bands.

The three galaxies chosen for this sample are NGC 55, NGC 3109, and IC 5152 (see Table 1). All three are low-metallicity ($12\% Z_{\odot} \leq Z \leq 49\% Z_{\odot}$; see below) dwarf galaxies located within 2 Mpc. These systems were chosen for their proximity (maximizing spatial resolution) and for their ongoing star formation. Further, the metallicities of the galaxies in this sample bracket the aforementioned empirical PAH transition metallicity. While our sample size is modest, the spatially resolved data for each system provide new insights into the variations of PAH intensities in metal-poor environments.

This research uses the Infrared Spectrograph (IRS; Houck et al. 2004) Short-Low module to create spectral maps of the high IR surface brightness regions of the sample galaxies. IRS is able to cleanly separate the $6.2 \mu\text{m}$, $7.7 \mu\text{m}$, and $8.6 \mu\text{m}$ PAH features, as well as to differentiate between the PAH features and the underlying warm dust continuum. We examine the radiances of PAH features across the observed regions of the target galaxies. From these measurements, combined with extensive ancillary data from the UV through the mid-infrared, it is possible to correlate emission from various gaseous and stellar components. We can then constrain some of the factors suspected of affecting the intensity of PAH emission (e.g., radiation field hardness, PAH molecule size distribution).

2. Observations and Data Reduction

Data were obtained using *Spitzer*/IRS for general observer (GO) Program 40457 (PI Skillman). Spectra were acquired with the Short-Low (SL) slit ($5\text{--}15 \mu\text{m}$) for all three targets. Mapping used parallel steps of size $28.35''$, and perpendicular steps of size $1.85''$. NGC 55 was observed for a total of 7 hours, using one cycle of ramp duration 14 seconds on 6 parallel and 60 perpendicular steps. 6.2 hours were required to observe IC 5152 with one 60 second ramp on 2 parallel steps and 50 perpendicular steps. NGC 3109 also required 6.2 hours for two cycles of 60 second ramps on one parallel step and 70 perpendicular steps. Observations were completed between November 2007 and January 2008. IRS mapping footprints can be seen in Figure 1, where we overlay the IRS spectral map placement on IRAC $8 \mu\text{m}$ images. Note that we targeted the areas of highest IR surface brightness.

Basic calibrated data (BCD) from the *Spitzer* pipeline has been flat-fielded and converted to specific intensity units (MJy sr^{-1}). We use the CUbe Builder for IRS Spectral Mapping (CUBISM; Smith et al. 2007) for much of the analysis in this investigation. First, the data were cleaned using a 4-sigma cut, removing hot pixels. Further cleaning was then done by

hand to assure data quality.

For IC 5152 and NGC 3109, dedicated sky observations were used for background subtraction. NGC 55 had a sufficient number of off-target BCD sets that could be used for background subtraction. These off-target BCDs were judged to be cleaner than the dedicated sky data, since more and cleaner astronomical observation requests (AORs) from the target data set were available for background subtraction than from the dedicated sky observations.

For stitching together spectral data from the first and second order of the slit, a low order polynomial was fitted to the SL2 data in the region of overlap. Specific intensity values were then averaged in the region of overlap. All data were then smoothed over three pixels. Fitting errors were small, so total errors are presented, except in the region of overlap, where the fitting errors were significant. For NGC 55, NGC 3109, and IC 5152, average errors were 2%, 17%, and 10% respectively. The only areas of significantly higher error were in the region of overlap, where errors ranged up to three times higher than the averages outside of the overlap region.

The program PAHFIT (Smith et al. 2007) was used to fit the spectra and to extract numerical values describing PAH features and emission lines. PAHFIT was trained on a number of high S/N ratio galaxies, and uses a simple, physically motivated model that includes dust continuum, starlight, emission lines and bands, and extinction. Most components are fixed, including starlight temperature (5000 K) and central wavelengths and widths of dust features. The dust continuum is based on eight components represented by modified blackbodies at a range of temperatures between 35 and 300 K. These components are allowed to be zero, though not negative. The extinction is given as a power law with silicate features peaking at $9.7 \mu\text{m}$ and $18 \mu\text{m}$. The line feature wavelengths are allowed to vary by $0.05 \mu\text{m}$, and line widths are allowed to vary by 10% from their default values. Spectral lines are represented by Gaussian profiles, while dust features are represented by Drude profiles, both individual and blended. Because of the highly blended nature of many of the PAH features, the PAHFIT “Main Power Feature” program was used to combine the most heavily blended features into complexes by adding individual features across a specified wavelength interval. PAHFIT is designed to use combined SL and LL *Spitzer* data in order to accurately reconstruct the continuum emission; unfortunately, LL data are unavailable for our sample galaxies. Therefore, while the total continuum appears to fit the spectra quite well, some caution should be used in interpreting the continuum fits themselves (especially at wavelengths outside of the 5.5–14.5 μm range covered by the IRS SL1 and SL2 slits).

PAHFIT fits the spectra by minimizing the global χ^2 , and returns statistical uncertainties. Global χ^2 values for NGC 55, NGC 3109, and IC 5152 are 59.122, 5.76, and 5.20,

respectively. Average uncertainties in dust features were 2%, 17%, and 7% for the global fits for NGC 55, NGC 3109, and IC 5152, respectively.

In addition to 1D spectra, 2D spectral maps from various wavelength regions were also generated using CUBISM’s mapping feature. This procedure allows the user to specify “peak” and “continuum” wavelength intervals. CUBISM then subtracts the specified continuum from the peak, and creates a map of the resulting emission. For maps covering spectral regions between $7.4\ \mu\text{m}$ and $7.6\ \mu\text{m}$, the overlap region between SL1 and SL2, a more detailed method was needed. In this case, maps were extracted separately in each slit and averaged together in the area of overlap before being combined.

3. Global Comparisons

3.1. Galaxy Properties

As noted above, the galaxies in our sample were selected based on proximity and the presence of ongoing star formation. These three dwarf irregulars span a modest range in metallicity (~ 0.6 dex), but larger ranges in SFR, dynamical mass and absolute magnitude (Table 1). The ISM oxygen abundances have been determined through observations of H II regions. The temperature sensitive [O III] $\lambda 4363$ line was detected in each system, resulting in reliable abundance determinations. These abundances are $12 + \log(\text{O}/\text{H}) = 8.4 \pm 0.1$ for NGC 55 (Webster & Smith 1983), 7.92 ± 0.07 for IC 5152 (Lee et al. 2003a), and 7.74 ± 0.33 for NGC 3109 (Lee et al. 2003b).

Previous investigations have studied the luminosity of the $8\ \mu\text{m}$ PAH feature via imaging. Typically the IRAC band 1 or 2 images (at $3.6\ \mu\text{m}$ and $4.5\ \mu\text{m}$, respectively) are assumed to accurately represent the underlying stellar continuum; these images are scaled and subtracted from the IRAC $8\ \mu\text{m}$ image (see detailed discussion in Jackson et al. 2006). The resulting diffuse $8\ \mu\text{m}$ emission (which includes contributions from the $6.2\ \mu\text{m}$, $7.7\ \mu\text{m}$ and $8.6\ \mu\text{m}$ PAH features) in these systems scales approximately with the metallicity. NGC 3109 has the lowest gas-phase abundance ($\sim 12\% Z_{\odot}$) and the lowest total diffuse $8\ \mu\text{m}$ flux density ($0.06\ \text{Jy}$). IC 5152 is slightly more metal-rich ($\sim 18\% Z_{\odot}$) and harbors a larger total $8\ \mu\text{m}$ flux density ($0.16\ \text{Jy}$). Moving above the threshold metallicity ($12 + \log(\text{O}/\text{H}) \simeq 8.0$; Engelbracht et al. 2005), NGC 55 ($\sim 49\% Z_{\odot}$) is an order of magnitude brighter in the IRAC $8\ \mu\text{m}$ band ($1.4\ \text{Jy}$). Note by examining Figure 1 that our IRS spectral maps cover only the regions of highest surface brightness $8\ \mu\text{m}$ emission; the IRS field of view encompasses 41%, 18%, and 57% of the intensity in the IRAC $8\ \mu\text{m}$ field of view for NGC 55, NGC 3109, and IC 5152, respectively (with no foreground star correction or continuum subtraction applied).

While the scaling of PAH emission (as measured by the diffuse 8 μm flux density) with metallicity is expected based on recent empirical results, the comparisons with other global parameters are more ambiguous. The system with the smallest dynamical mass and current SFR (IC 5152) is a factor of ~ 2 more luminous in the IRAC 8 μm band than NGC 3109. While the current SFRs in these two systems differ only at the $\sim 10\%$ level, it is perhaps more surprising that NGC 3109 is ~ 16 times more massive than IC 5152. Moving further upward in mass, NGC 55 is the most massive and metal-rich system in the sample. Its current SFR and diffuse 8 μm flux density are both more than an order of magnitude larger than in NGC 3109, although the mass and metallicity are only larger by a factor of ~ 3 . Taken together, this discussion highlights the complexity of these multiple inter-related properties. While statistical correlations exist between some parameters in large samples (e.g., Rosenberg et al. 2006), it is apparent that individual systems are complex composites of multiple factors. It is our aim to investigate these variations within three selected systems on a spatially resolved basis in the present investigation. We thus hereafter use the term “global” to identify results or properties obtained by integrating spectra over the IRS fields of view as shown in Figure 1. These global results are separated from those attained by individually integrating over smaller regions within the field of view (see § 4).

3.2. Spectra

3.2.1. Comparing NGC 55, NGC 3109 and IC 5152

The global spectra shown in Figures 2, 3, and 4 were created by integrating the IRS specific intensity over the entire observed area of the galaxy for NGC 55, NGC 3109, and IC 5152, respectively. While these spectra vary significantly in total intensity and signal to noise ratio, the overall shapes show similar emission patterns. The most prominent features in all three galaxies are the 7.7 μm PAH feature (somewhat blended with the 8.6 μm PAH feature), the 11.3 μm PAH feature, and the blended feature composed of [Ne II] emission at 12.8 μm and the 12.6 μm PAH feature. The [S IV] feature at 10.5 μm is prominent in NGC 55, weak in IC 5152, and undetectable in NGC 3109.

The global spectra are fitted by PAHFIT and decomposed into multiple components, including the thermal dust continuum, stellar continuum, PAH features, and atomic and molecular emission lines. PAHFIT was set such that the central wavelengths and widths of the features were not allowed to vary between galaxies. These decomposed global spectra for NGC 55, NGC 3109, and IC 5152 are shown in Figures 5, 6, and 7, respectively. Multiple components contribute to each peak visible in the full fit. For example, using the global spectrum of NGC 55 (Figure 5; highest S/N) as a guide, the 7.7 μm PAH complex has

contributions from components at $7.6\ \mu\text{m}$ and $7.8\ \mu\text{m}$. Similarly, the minor contribution of the $8.3\ \mu\text{m}$ PAH feature is evident between the $8.6\ \mu\text{m}$ and $7.7\ \mu\text{m}$ complexes, and the $11.3\ \mu\text{m}$ complex separates into two features at 11.2 and $11.3\ \mu\text{m}$, respectively. We remind the reader that the PAHFIT Main Power Feature (see discussion in § 2) explicitly calculates radiances across these blended complexes.

Figures 5, 6, and 7 show that the monochromatic specific intensity at all frequencies is highest in NGC 55. It is interesting to note that the stellar continuum is weaker compared to the dust continuum in NGC 55 than in the other two systems; we attribute this to both a larger dust content and a higher star formation rate in NGC 55 than in NGC 3109 or IC 5152. We also note with interest that the fit for NGC 3109 shows contributions from $\text{H}_2\ \text{S}(5)$ and $[\text{Ar II}]$ at $6.86\ \mu\text{m}$ and $6.94\ \mu\text{m}$ respectively (though the errorbars are appreciable), features that are largely absent from the other two galaxies.

The absolute values for the extracted radiances (units of $\text{W m}^{-2} \text{sr}^{-1}$) of the PAH features and ionized atomic lines are given in Table 2. As noted above, NGC 55 has the largest PAH luminosity in our sample; it has $\gtrsim 5$ and $\gtrsim 10$ times higher radiances in each PAH feature than IC 5152 or NGC 3109, respectively. NGC 55 also has the highest ionized atomic line radiances (compare the $[\text{Ne II}]$ $12.8\ \mu\text{m}$ values). Given these properties, the appearance of the modest ionization potential $[\text{Ar II}]$ line ($15.76\ \text{eV}$; Cox 2000) in only NGC 3109 is not surprising. The other two systems have stronger radiation fields: the $[\text{S IV}]$ $10.5\ \mu\text{m}$ feature in NGC 55 has an ionization potential of $34.79\ \text{eV}$, and the $[\text{Ne II}]$ $12.8\ \mu\text{m}$ line in both NGC 55 and IC 5152 has an ionization potential of $21.56\ \text{eV}$. The PAH features overwhelm the $[\text{Ar II}]$ line in these systems.

We compare the ratios of the radiances of the four prominent PAH features in a global sense for each galaxy in Table 3. The global $(8.6\ \mu\text{m})/(11.3\ \mu\text{m})$ ratio is the same (0.58 ± 0.19) for all three galaxies within the measurement uncertainties. The $(6.2\ \mu\text{m})/(11.3\ \mu\text{m})$, $(7.7\ \mu\text{m})/(6.2\ \mu\text{m})$, and $(7.7\ \mu\text{m})/(11.3\ \mu\text{m})$ ratios have more significant scatter (factors as large as 3-4). It is not immediately clear why the $(8.6\ \mu\text{m})/(11.3\ \mu\text{m})$ ratio is the most stable across all three galaxies. Considering the small sample size, it is possible that the small dispersion is a coincidence. Since the $8.6\ \mu\text{m}$ and $11.3\ \mu\text{m}$ PAH features are postulated to have contributions from CH bending modes (though the CH contribution to the $8.6\ \mu\text{m}$ feature is weak when the PAH carriers are ionized; see § 1.1), the small dispersion in those bands could be due to the ionization state of the PAHs. However, as mentioned above, the hardness of the radiation field in these systems varies considerably on both the global and the local level. Further, differences in ionization state do not explain why statistically significant variations between other bands that arise due to the same type of mode in similar ionization states (e.g., the $(7.7\ \mu\text{m})/(6.2\ \mu\text{m})$ ratio, which is dominated by the CC stretching modes

when the carriers are ionized) are observed. The constancy of the global $(8.6\ \mu\text{m})/(11.3\ \mu\text{m})$ ratio is thus likely due, at least in part, to a similar grain size distribution in this sample.

3.2.2. Comparing with Other Galaxies

Previous investigations have examined the variations (or lack thereof) in PAH/PAH ratios both globally among galaxies (e.g., Smith et al. 2007; Galliano et al. 2008; Hunt et al. 2010) and on a spatially resolved basis within galaxies (e.g., Galliano et al. 2008; Gordon et al. 2008). From these works, evidence is mounting that the relative intensities of the major PAH features are remarkably uniform, even across a wide range of local and global environments. The Smith et al. (2007) and Galliano et al. (2008) samples include a wide variety of sources (spirals, AGNs, dwarfs, H II regions); the Hunt et al. (2010) sample is composed entirely of blue compact dwarfs (BCDs); the Gordon et al. (2008) study probes individual H II regions in M 101. Such a collection of environments harbors a wide range of stellar populations, current SFRs, metal and dust contents, and large-scale dynamical processes. It would then be expected that the relative radiances of ionized ($6.2\ \mu\text{m}$, $7.7\ \mu\text{m}$ and $8.6\ \mu\text{m}$) versus neutral ($11.3\ \mu\text{m}$), and large versus small (in the same ionization state; e.g., $8.6\ \mu\text{m}$ versus $6.2\ \mu\text{m}$), PAH features would also vary considerably.

To examine both theories (grain size and ionization state) across this broad sample of environments, we plot in Figure 8 the three galaxies in this sample, the inner few kiloparsecs of a subset of SINGS galaxies from Smith et al. (2007), a wide range of galaxy types from Galliano et al. (2008), the sample of BCDs from Hunt et al. (2010), and the star formation regions in M 101 studied by Gordon et al. (2008). This plot is designed to show contributions from larger PAH molecules increasing up the y axis, and contributions from ionized (as compared to neutral) PAH molecules increasing along the x axis. All data represented were decomposed using PAHFIT, with the exception of the data points from Galliano et al. (2008), who used their own spectral decomposition method (in their study, Galliano et al. 2008 use two fitting methods, Spline and Lorentzian; we present only the Lorentzian method, as it more closely approximates the PAHFIT method). Sources were only included on our plot if the radiances of all four PAH features were available. We stress that the plot contains information about both entire galaxies (e.g., the BCDs) and individual regions within galaxies. Further, the data acquisition techniques (e.g., spectral mapping versus single pointing), analysis techniques (see above), and sensitivities may differ from one data point to another. While we remain mindful of these caveats, this collection of data represents, to our knowledge, all currently available information on the radiances of the $6.2\ \mu\text{m}$, $7.7\ \mu\text{m}$ and $8.6\ \mu\text{m}$ PAH features over a range of ambient metallicities within nearby galaxies.

We find that our three galaxies nicely fit within the overall trend established by the larger (and broader) samples, which on the whole show a minimal range in size distribution across an order of magnitude in ionization state (though outliers do exist; see the caption of Figure 8). This implies that a more or less constant grain size distribution exists over the appreciable range in ionization fraction covered by this sample. Considering the three galaxies in the present study (shown in red in Figure 8), NGC 55 falls in the center of the locus of points from the larger compilation; this is not surprising, given its comparatively large mass, metallicity, and dust content. IC 5152 also falls within the larger distribution, though at a lower ionization index than NGC 55. It may seem surprising that NGC 3109 appears at the highest ionization index (i.e., largest global $(7.7 \mu\text{m})/(11.3 \mu\text{m})$ ratio) in this plot; however, this is easily interpreted as its comparatively low S/N spectrum being heavily weighted toward the region of highest IR surface brightness (and thus most intense radiation field; we return to this point in § 4).

Taken as a whole, Figure 8 is evidence for a similar PAH size distribution in spirals, AGN, dwarfs, and H II regions. This suggests that the emission properties of the PAH carriers are more significantly affected by their local environment than by the past growth/destruction history (in agreement with previous works, e.g., Jackson et al. 2006). It also indicates that the growth/destruction history is not measurably affected by local effects, and that instead the grain size distribution, if not varying or affected on the local level, is instead affected by larger scale, more long-term processes. It is also apparent that dwarf galaxies constitute some of the most extreme outliers from the general trend seen in Figure 8: the BCDs from the Hunt et al. (2010) sample (shown in green) appear at the extrema of the locus of points from the Smith et al. (2007) and Galliano et al. (2008) studies, suggesting a wide range in global ionization indices in these dwarfs.

One may be tempted to ascribe the extremal ratios found in some of (but not all) the dwarf galaxies to metallicity effects. To examine this possibility, we plot in Figure 9 the global $(8.6 \mu\text{m})/(6.2 \mu\text{m})$ and $(7.7 \mu\text{m})/(11.3 \mu\text{m})$ ratios versus gas-phase oxygen abundances for a subset of the systems in Figure 8. In creating this plot, we implicitly assume no abundance gradients in the dwarfs, and we explicitly exclude global values for spirals, as they have well-documented abundance gradients. We do, however, include the measurements of individual H II regions in M 101 (each with abundance measurements) presented by Gordon et al. (2008). In interpreting this plot, we remain mindful that the dataset is inhomogeneous in the sense that the local conditions within individual star formation regions of a spiral disk will be quite distinct from those within a dwarf galaxy. We also stress again that the high global $(7.7 \mu\text{m})/(11.3 \mu\text{m})$ ratio in NGC 3109 is heavily weighted toward the region of highest IR surface brightness. With these caveats in mind, we find only very weak evidence for a trend of increasing grain size or ionization index with increasing metal abundance.

This is in agreement with previous studies (e.g., Jackson et al. 2006; Rosenberg et al. 2006; Gordon et al. 2008), where the effect of metallicity has been found to be secondary to other factors in controlling the intensities of PAH emission features. While the total amount of metals in a galaxy is clearly an important property in governing the intensity of PAH emission (Engelbracht et al. 2005, 2008), evidence shows that the relative intensities of the PAH features show a remarkable degree of uniformity in the systems considered here.

4. Spatially Resolved Emission

In order to examine the comparative spatial distributions of dust, gas, stellar populations, and radiation field strengths in our sample galaxies, images are shown at various wavelengths in Figures 10, 11, and 12 for NGC 55, NGC 3109, and IC 5152, respectively. Here we exploit our mapping observational strategy (see § 2). Using the global spectrum of each galaxy, individual spectral regions are selected that bracket PAH or emission lines of interest. The underlying continuum is removed using areas of the spectrum outside the feature (we note the difficulty of accurate continuum subtraction for some of the wide PAH features, especially the blended features in the $7\ \mu\text{m} - 9\ \mu\text{m}$ range). The spatial location of the regions that contribute are known; a map is then constructed of the emission in a given wavelength interval (see Smith et al. 2007b for details). The complexity of the spectrum of each system (see Figures 2, 3, and 4) requires fine-tuning of the spectral extraction regions for each feature individually. We explicitly list the wavelength intervals over which the emission maps are created for each system in Table 4.

Panels (i), (j), and (k) of Figures 10, 11, and 12 show images created from the IRS data. The spatial distributions of IRS 11.3 μm (see panel j of each figure) and broad 8 μm (integrated from $7.288\ \mu\text{m} - 8.900\ \mu\text{m}$ in all systems; note that this includes contributions from both the 7.7 μm and the 8.6 μm PAH complexes; see panel i of each figure) emission correlate well in all three galaxies. The IRAC and IRS 8 μm maps also agree in most areas; the small observed differences are most likely due to the larger bandwidth of the IRAC 8 μm filter (extending from $\sim 6.4\ \mu\text{m} - \sim 9.4\ \mu\text{m}$). As a check on the quality of the absolute flux calibration of the IRS spectra, we explicitly compared the total flux density in the IRAC 8 μm band with the total flux density integrated over the matching IRAC bandpass in the IRS spectrum of each galaxy; while these images are not shown in Figures 10–12, the resulting flux densities agree at the 8%, 13%, and 17% levels for NGC 55, IC 5152, and NGC 3109, respectively.

There is very good spatial correlation between emission from PAH features and ionized gas as indicated by [Ne II] emission (see panel k of each figure) in NGC 55 and IC 5152. This

immediately suggests that the PAH emission is arising from regions with comparatively hard radiation fields (recall that the ionization potential of [Ne II] is ~ 21.6 eV) in these systems. There is a much poorer spatial agreement between [Ne II] and PAH emission in NGC 3109.

It is interesting to note that in only a few regions in these galaxies do areas of high surface brightness UV emission coincide with areas of high surface brightness PAH emission. There are locations in each system that are UV-bright and PAH-dim (arguing for minimal extinction) as well as regions that have high PAH surface brightnesses but little observed UV or optical emission (arguing for pronounced local extinction). Examining each system from the UV to $4.5\ \mu\text{m}$ in Figures 10, 11 and 12, we conclude that the multiwavelength characteristics of NGC 55 and NGC 3109 are consistent with variable extinction of up to a few magnitudes in the UV; both systems show good agreement between $11.3\ \mu\text{m}$ PAH surface brightness and $4.5\ \mu\text{m}$ morphology. IC 5152 is more challenging to interpret: its near-infrared stellar population bears a strikingly different morphology than the PAH or [Ne II] emission. This can be interpreted as more severe localized extinction than in NGC 55 or NGC 3109; such variations have been observed in dwarf galaxies in previous works (e.g., Cannon et al. 2006). These implied optical and UV extinctions are in agreement with the global values derived by Lee et al. (2009), albeit with significant internal variations.

In all three galaxies, we examine PAH ratios for individual sources that are spatially resolved in our spectral image data cubes. Spectra were extracted from CUBISM maps using circular regions of 52.5 pc radius. These extraction regions can be seen in Figures 13 (NGC 55), 14 (NGC 3109), and 15 (IC 5152). 52.5 pc is four times the smallest spatial resolution possible with the data, or four pixels wide on the IRS map of NGC 55 ($D = 2.17$ Mpc, the most distant system). At $8.6\ \mu\text{m}$, *Spitzer's* diffraction limit is $2.55''$; 52.5 pc corresponds to $5.0''$ at the distance of the NGC 55. For NGC 3109 and IC 5152, the extraction regions are $8.1''$ and $5.5''$, respectively. Extraction regions were chosen to be the same physical size in each galaxy for optimal comparison of features. 52.5 pc radius regions were judged to best fit physical variations in structure across the varying angular size of all three galaxies; further, 52.5 pc is large enough to analyze on NGC 55, but small enough to allow multiple regions to be extracted from NGC 3109 and IC 5152. The extracted spectrum of each region was then fitted with PAHFIT to derive PAH feature and emission line radiances. The results of these fits are shown in Tables 5, 6, 7, 8, 9, and 10, and discussed in detail in § 4.1, § 4.2, and § 4.3 below.

PAH band variations are also examined on a pixel by pixel basis; we show these results in Figures 16 and 17. The data included in these plots were not calculated by PAHFIT. Instead, spectral maps were extracted from CUBISM; individual pixel specific intensities, integrated specific intensities within the apertures described above (see Figures 13, 14, and

15), and integrated global specific intensities were then derived from these images. The reported errors are taken directly from the error maps as produced by CUBISM. Only pixels with a S/N ratio of 3 or higher are included in the pixel-by-pixel analysis; all pixels in a given region are included for the region and global values.

Figures 16 and 17 show that the $(7.7 \mu\text{m})/(11.3 \mu\text{m})$ PAH radiance ratios span only a factor of ~ 5 within each of these galaxies. Interestingly, for NGC 55 and IC 5152, the regions are in good agreement with the pixel data. However, for NGC 3109, a marked shift to lower $(7.7 \mu\text{m})/(11.3 \mu\text{m})$ ratios is seen for the integrated regions compared to the individual pixel values. This is due to the uncertainty cut on the pixels, which removes low S/N pixels from the data. This means that the extraction regions, which had no uncertainty cut applied, have the potential to contain pixels of a much lower specific intensity than is possible in the individual pixel data. Conversely, the individual pixels are therefore weighted towards higher surface brightness regions of the galaxy in a way the extraction regions are not. This difference is most notable in low S/N regions like Region 2. Region 4, the highest surface brightness region in NGC 3109, is well within the average range of the rest of the pixels. Examination of Figure 11 shows more diffuse $11.3 \mu\text{m}$ emission than other bands in NGC 3109, including the IRS 8 μm band, which encompasses the $7.7 \mu\text{m}$ PAH feature. From this we conclude that integrating over lower surface brightness regions would indeed produce a larger contribution from $11.3 \mu\text{m}$ compared to $7.7 \mu\text{m}$ emission, leading to a smaller ratio of these two values.

The small changes (a factor of ~ 5 , or just larger than the associated uncertainties for most regions) in the $(7.7 \mu\text{m})/(11.3 \mu\text{m})$ PAH radiance ratios can be interpreted as a relatively minor variation of the ionization index (i.e., radiation field strength) within a given galaxy. For NGC 55 and IC 5152, this is to be expected from examination of Figures 10 and 12. The agreement in morphology between the [Ne II] emission line and the IRS 8 μm and $11.3 \mu\text{m}$ PAH bands shows that the latter two are primarily arising in regions rich in energetic photons. The interpretation of the NGC 3109 plot is more ambiguous, primarily because there are so many fewer pixels that contribute above the 3σ level compared to the two more massive systems. However, at face value, the variation of the $(7.7 \mu\text{m})/(11.3 \mu\text{m})$ PAH radiance ratio across NGC 3109 implies that the radiation field strength is high in one specific region (where the individual pixels achieve a S/N ratio above 3) and lower throughout most of the system. This is also apparent by examining Figure 11.

Two diagnostics of the PAH size distribution are plotted against the $(7.7 \mu\text{m})/(11.3 \mu\text{m})$ PAH radiance ratio in Figures 16 and 17, the former via the $(7.7 \mu\text{m})/(6.2 \mu\text{m})$ PAH radiance ratio and the latter via the $(8.6 \mu\text{m})/(6.2 \mu\text{m})$ PAH radiance ratio. Note that both of these ratios are dominated by the CC stretching modes in regions where the PAH carriers

are ionized (see the distributions of [Ne II] emission throughout each system in Figures 10, 11 and 12). Recall that the $7.7\ \mu\text{m}$ PAH feature arises from a mixed population of large and small carriers, so the interpretation of the $(7.7\ \mu\text{m})/(6.2\ \mu\text{m})$ ratio as sensitive only to the PAH size distribution should be treated with more caution than the $(8.6\ \mu\text{m})/(6.2\ \mu\text{m})$ ratio. From these plots we see that NGC 55 shows a trend of larger grain sizes (i.e., larger ordinate values) in regions of harder radiation field (larger abscissa values), with a more transparent correlation using the larger difference in grain size (i.e., in the $(8.6\ \mu\text{m})/(6.2\ \mu\text{m})$ plot). IC 5152 shows a slight trend in the same sense but the signature is weaker than in NGC 55. NGC 3109 shows a weak trend in the opposite sense. We again stress that the region and global radiances in these figures have no minimum specific intensity threshold; hence the reality of the trend in NGC 3109 should be interpreted with caution.

In summary, Figures 16 and 17 show variations of radiation field strength and PAH carrier size distributions on a spatially resolved basis. While very weak trends can be inferred in these data, they are nonetheless consistent with an interpretation of very little variation in grain size distribution as a function of radiation field strength. This would seem to indicate that the distribution of PAH grain sizes are long lived, and not significantly affected by local phenomena. Stated differently, the constancy of the PAH/PAH ratios seen amongst galaxies (see detailed discussion in § 3.2 above) appears to extend down to the spatially resolved level within individual galaxies as well. While our study has pre-selected regions that are IR-bright within these dwarfs (and thus potentially having homogeneous characteristics), the variations of PAH feature radiances on these spatial scales are very similar to the variations seen on global scales.

4.1. NGC 55

Data for nineteen circular regions with a radius of 52.5 pc (some of them unavoidably containing areas of overlap) were extracted across the observed region of the galaxy (see Figure 13), and their extracted radiances are shown in Table 5. As expected based on the results discussed above and shown in Figures 16 and 17, we find very few statistically significant deviations of PAH/PAH radiance ratios derived in these apertures throughout NGC 55. Table 5 shows the weighted mean values of the $(6.2\ \mu\text{m})/(11.3\ \mu\text{m})$, $(7.7\ \mu\text{m})/(11.3\ \mu\text{m})$, $(8.6\ \mu\text{m})/(11.3\ \mu\text{m})$, $(7.7\ \mu\text{m})/(6.2\ \mu\text{m})$ and $(8.6\ \mu\text{m})/(6.2\ \mu\text{m})$ radiance ratios and the standard deviation across this sample. Of the 95 ratios given in the table, we identify 11 ratios that deviate at more than the 2σ level; no variations at the 3σ level or larger are identified. Only two regions are identified as having variations in more than one band: Region 2 has $\sim 2\sigma$ variations in all ratios except $(6.2\ \mu\text{m})/(11.3\ \mu\text{m})$, while Region 16 has

$\sim 2\sigma$ variations in the $(7.7\ \mu\text{m})/(11.3\ \mu\text{m})$, $(8.6\ \mu\text{m})/(11.3\ \mu\text{m})$, and $(7.7\ \mu\text{m})/(6.2\ \mu\text{m})$ radiance ratios.

We compare the radiances of PAH features with emission lines and broad-band MIPS $24\ \mu\text{m}$ dust continuum in Table 6. The radiance of the [Ne II] emission line compared to that of either a neutral ($11.3\ \mu\text{m}$) or an ionized ($8.6\ \mu\text{m}$) PAH emission feature show very few statistically significant variations within NGC 55. Similarly, the ratio of $24\ \mu\text{m}$ to PAH radiances is fairly uniform across this galaxy, though the standard deviation is much larger.

We draw attention to some interesting complexities in the data in Table 6. First, Region 10 is extremely bright throughout the MIR, and especially so at $24\ \mu\text{m}$ (compare Figures 10 and 13); it has the largest $(24\ \mu\text{m})/(11.3\ \mu\text{m})$ ratio (a $>3\sigma$ deviation from the average) and one of the highest ratios of $24\ \mu\text{m}$ radiance to the $8.6\ \mu\text{m}$ PAH band. It is luminous in the UV and coincident with a high-surface brightness optical cluster. However, its ratio of [Ne II] to PAH radiance is average. Region 16 is also luminous at $24\ \mu\text{m}$, but contains no UV or optical counterpart and again has average [Ne II] emission line ratios compared to the PAH features. Finally, Region 19 is luminous at all wavelengths (see Figure 10) and has the largest [Ne II] to PAH ratio in NGC 55. Thus, although the conditions within individual regions in NGC 55 are diverse, we find no statistically significant variations of PAH/PAH radiance ratios in the observed regions of NGC 55.

4.2. NGC 3109

We examine four $52.5\ \text{pc}$ radius apertures in NGC 3109. The low S/N ratio throughout much of the observed region limits our exploration to only those areas that are comparatively IR-bright (see Figure 11). Negligible scatter is seen in the PAH/PAH radiance ratios for these regions, as seen in Table 7; only one aperture deviates from the weighted mean at the 2σ significance level (the $(6.2\ \mu\text{m})/(11.3\ \mu\text{m})$ ratio for Region 4). This is in marked contrast to the very significant variations seen in the ratio of $24\ \mu\text{m}$ to PAH radiance in these four regions of the galaxy. While the weighted mean in Table 8 is affected by the difference in the errorbars over the small number of apertures, it is clear that Regions 1 and 4 have very different properties.

An examination of Figure 11 highlights curious differences between these two regions. Region 1 contains very weak [Ne II] $12.8\ \mu\text{m}$ emission; it clearly harbors an embedded IR source, since it has no associated UV emission, is fairly weak in the IRAC $8\ \mu\text{m}$ band, but very luminous at $24\ \mu\text{m}$. This suggests a cool thermal dust component at this location. Taken together, these properties suggest that the radiation field strength is low at the location of

Region 1 and that the PAHs present have a significant neutral component.

Regions 3 and 4 are in close physical proximity and present an interesting local environment with significant variations over small physical scales. Region 4 is very bright in the IRAC 8 μm band and is coincident with a high surface brightness optical cluster. Region 3 is much fainter at 8 μm , yet it has the largest $[\text{Ne II}]/(\text{PAH})$ ratios of any of the regions in NGC 3109.

Despite these dramatic changes in environmental properties, the ratios of PAH features presented in Table 7 are statistically indistinguishable. Even a cursory examination of the panels in Figure 11 highlights the complexity of the relationship between PAH emission and local properties in galaxies (e.g., slope of the local infrared spectral energy distribution (SED), UV intensity, infrared emission line radiance, etc.). The data for NGC 3109, while only available for selected regions, provides support for the hypothesis of constant PAH ratios within dwarf galaxies.

4.3. IC 5152

We examine ten 52.5 pc radius apertures within the observed region of IC 5152. The extracted PAH/PAH radiance ratios are presented in Table 9. Of the 50 ratios shown in that table, only 1 (the (7.7 μm)/(6.2 μm) ratio for Region 5) shows a deviance from the weighted mean at even the 2σ level. Similarly, as shown in Table 10, there are few variations of the ratios of $[\text{Ne II}]$ to PAH emission, or of the ratios of 24 μm to PAH emission, that are statistically significant.

The constancy of these ratios again arises from a wide variety of local conditions within IC 5152. In the most extreme example in our limited sample, the IR, optical, and UV morphologies are decidedly different in IC 5152. Most of the UV clusters have associated IR emission, but the converse is not true; a significant IR component exists in this system that has no associated UV, optical or near-infrared emission. Similarly, the dominant cluster in the UV, optical and near-infrared has very little associated PAH or dust emission. This dichotomy has been seen previously in nearby dwarfs (e.g., Cannon et al. 2006) and is suggestive of a substantial embedded star-forming population in IC 5152.

Considering the regions with extracted radiances, Region 10 contains the brightest 24 μm source in the galaxy; it is coincident with a UV cluster and is bright in the 8 μm and 11.3 μm PAH bands, as well as luminous in the $[\text{Ne II}]$ emission line. While its 24 μm to PAH ratios are high, the ratios of the PAH emission features themselves are indistinguishable from other regions in IC 5152. Region 8 has high surface brightnesses in each of the panels

of Figure 12, including in the [Ne II] emission line. Again, its PAH/PAH ratios appear to be average compared to others within the galaxy. At the opposite extreme is Region 6, which samples a region of low IR surface brightness. While diffuse UV emission is coincident with this aperture, its PAH/PAH radiance ratios again appear normal.

Taken as a whole, the apertures in IC 5152 lead to the same conclusions as those for NGC 55 and NGC 3109. While substantial local environmental changes occur within the dwarf galaxies of this limited sample, those changes do not produce measurable differences in the intensities of the major PAH bands. The radiance ratios of these prominent MIR features appear to be insensitive to a wide variety of local environmental factors.

5. Conclusions

Three nearby ($D \lesssim 2$ Mpc), low-metallicity ($12\% Z_{\odot} \leq Z \leq 49\% Z_{\odot}$) dwarf galaxies (NGC 55, NGC 3109, and IC 5152) were observed using the *Spitzer*/IRS Short-Low module in spectral mapping mode. We examine the resulting spectra on both global (integrated over the entire field of view, which targets the regions of high IR surface brightness) and spatially resolved scales. These data allow us to study the relative intensities of the four prominent PAH bands at $6.2 \mu\text{m}$, $7.7 \mu\text{m}$, $8.6 \mu\text{m}$ and $11.3 \mu\text{m}$.

Investigation of the global properties of our galaxies reveals the complex interactions that influence the intensity of PAH emission in galaxies. While metallicity does correlate with PAH emission (with a transition metallicity occurring at $\sim 25\% Z_{\odot}$), our examination of these three galaxies provides evidence that other global parameters (e.g., mass, metallicity, current SFR) also affect the nature of PAH emission.

Over the full area of our spectral maps, the relative ratios of most PAH bands vary by a factor of 3-4 across our sample. The exception is the ratio of $(8.6 \mu\text{m})/(11.3 \mu\text{m})$ radiances, which is constant on the global level for all three systems. Given that the radiation field strength shows considerable variation across this sample (with the comparatively metal-rich ISM of NGC 55 showing widespread [Ne II] emission, and the metal-poor ISM of NGC 3109 having only a few isolated regions of ionized gas), we interpret the constant value of the $(8.6 \mu\text{m})/(11.3 \mu\text{m})$ PAH ratio as evidence for a similar PAH size distribution across our sample. It then follows that if the PAH size distribution is similar across our sample, that the grain size distribution must be fairly long-lived and stable.

We compare the global PAH radiance ratios in our sample galaxies with a collection of similar measurements that probe a wide variety of sources from Smith et al. (2007), Galliano et al. (2008), Gordon et al. (2008), and Hunt et al. (2010). From this comparison,

we see evidence for a similar PAH size distribution across the range of objects explored, which includes spirals, AGN, dwarfs, and H II regions. The ionization indices vary significantly within these different sources. Taken together, these properties suggest that the local environment has a greater impact on the intensity of PAH emission than does the metallicity or the history of PAH formation/destruction in a given galaxy or region.

We also examine PAH emission on a spatially resolved basis by extracting maps of PAH features and emission lines in our sample galaxies. Examining both individual pixels (in regions of high S/N) and apertures of physical radius 52.5 pc, we find that the $(7.7\ \mu\text{m})/(11.3\ \mu\text{m})$ ratio (a probe of ionization index or radiation field strength) varies by a factor of ~ 5 across our sample. The grain size distribution (using the $(8.6\ \mu\text{m})/(6.2\ \mu\text{m})$ ratio as a diagnostic) shows only very minor variations over this range. This agrees with the interpretations found for other galaxies and suggests that there is very little change in the PAH carrier size distribution as a function of radiation field strength.

Previous works have suggested that the relative intensities of the main PAH features are essentially constant within a given galaxy (see references in § 3 and 4 above). Our examination of the ISM in the three dwarf galaxies of this sample supports this interpretation. In comparing the PAH/PAH ratios at a spatial resolution of 52.5 pc, we find very few regions that display statistically significant deviations from the mean within a given system (no variations exceed the 3.5σ level, and most are at the 2σ level or lower). In contrast to the diverse environmental variations seen between regions in our sample, the PAH band ratios are constant within each galaxy.

The apparently simple conclusions of this work mask a great deal of complexity in the canonically “simple” ISM of dwarf galaxies. The uniformity of metal abundance in these systems is well-documented but has not yet been explained. The present work suggests that this uniformity also extends to the properties of the carriers of the PAH bands. When examining each of these systems, we find a remarkably wide variety of physical conditions: some star formation regions are UV-bright while others are deeply embedded; some regions have widespread ionizing photons while others are apparently quiescent; some regions are dominated by the red stellar continuum while others have SEDs that rise steeply toward the far-IR. In response to these diverse local conditions, the intensity of the PAH emission features do in fact change markedly, in line with expectations based on the strength of the local radiation field and the metallicity. However, the relative intensities of these PAH bands appear to be strikingly uniform over these variable local conditions.

This work is based on observations made with the *Spitzer Space Telescope*, which is operated by the Jet Propulsion Laboratory, California Institute of Technology, under a con-

tract with NASA. Support for this work was provided by NASA through contract 1321212, issued by JPL/Caltech to J.M.C. at Macalester College. RDG was supported in part by NASA through contracts 1256406 and 1215746 issued by JPL/Caltech to the University of Minnesota. This research has made use of the NASA/IPAC Extragalactic Database (NED) which is operated by the Jet Propulsion Laboratory, California Institute of Technology, under contract with the National Aeronautics and Space Administration, and NASA’s Astrophysics Data System. This publication has made use of data products from the Two Micron All Sky Survey, which is a joint project of the University of Massachusetts and the Infrared Processing and Analysis Center/California Institute of Technology, funded by the National Aeronautics and Space Administration and the National Science Foundation. We would like to acknowledge Daniel A. Dale, J.D. Smith, Thomas Varberg, and the *Spitzer* Science Center for helpful discussions and support. Finally, we thank the anonymous referee for a careful and insightful report that improved this manuscript.

REFERENCES

- Allamandola, L. J., Hudgins, D. M., & Sandford, S. A. 1999, *ApJ*, 511, L115
- Allamandola, L. J., Tielens, A. G. G. M., & Barker, J. R. 1989, *ApJS*, 71, 733
- Bakes, E. L. O., Tielens, A. G. G. M., & Bauschlicher, C. W., Jr. 2001, *ApJ*, 556, 501
- Bauschlicher, C. W., Jr. 2002, *ApJ*, 564, 782
- Bauschlicher, C. W., Peeters, E., & Allamandola, L. J. 2009, *ApJ*, 697, 311
- Bauschlicher, C. W., Jr., Peeters, E., & Allamandola, L. J. 2008, *ApJ*, 678, 316
- Cannon, J. M., et al. 2006, *ApJ*, 647, 293
- Cannon, J. M., et al. 2006, *ApJ*, 652, 1170
- Compiègne, M., Abergel, A., Verstraete, L., Reach, W. T., Habart, E., Smith, J. D., Boulanger, F., & Joblin, C. 2007, *A&A*, 471, 205
- Cox, A. N. 2000, *Allen’s Astrophysical Quantities*
- Dale, D. A., et al. 2009, *ApJ*, 693, 1821
- Draine, B. T., & Li, A. 2007, *ApJ*, 657, 810
- Engelbracht, C. W., Gordon, K. D., Rieke, G. H., Werner, M. W., Dale, D. A., & Latter, W. B. 2005, *ApJ*, 628, L29
- Engelbracht, C. W., Rieke, G. H., Gordon, K. D., Smith, J.-D. T., Werner, M. W., Moustakas, J., Willmer, C. N. A., & Vanzì, L. 2008, *ApJ*, 678, 804
- Galliano, F., Madden, S. C., Tielens, A. G. G. M., Peeters, E., & Jones, A. P. 2008, *ApJ*, 679, 310
- Giard, M., Lamarre, J. M., Pajot, F., & Serra, G. 1994, *A&A*, 286, 203
- Gordon, K. D., Engelbracht, C. W., Rieke, G. H., Misselt, K. A., Smith, J.-D. T., & Kennicutt, R. C., Jr. 2008, *ApJ*, 682, 336
- Helou, G., Lu, N. Y., Werner, M. W., Malhotra, S., & Silbermann, N. 2000, *ApJ*, 532, L21
- Helou, G., Malhotra, S., Hollenbach, D. J., Dale, D. A., & Contursi, A. 2001, *ApJ*, 548, L73
- Helou, G., et al. 2004, *ApJS*, 154, 253

- Hogg, D. W., Tremonti, C. A., Blanton, M. R., Finkbeiner, D. P., Padmanabhan, N., Quintero, A. D., Schlegel, D. J., & Wherry, N. 2005, *ApJ*, 624, 162
- Houck, J. R., et al. 2004, *ApJS*, 154, 18
- Hunt, L. K., Thuan, T. X., Izotov, Y. I., & Sauvage, M. 2010, *ApJ*, 712, 164
- Jackson, D. C., Cannon, J. M., Skillman, E. D., Lee, H., Gehrz, R. D., Woodward, C. E., & Polonski, E. 2006, *ApJ*, 646, 192
- Jarrett, T. H., Chester, T., Cutri, R., Schneider, S. E., & Huchra, J. P. 2003, *AJ*, 125, 525
- Kennicutt, R. C., Jr., et al. 2003, *PASP*, 115, 928
- Kim, H.-S., & Saykally, R. J. 2002, *ApJS*, 143, 455
- Kobulnicky, H. A., & Skillman, E. D. 1996, *ApJ*, 471, 211
- Kobulnicky, H. A., & Skillman, E. D. 1997, *ApJ*, 489, 636
- Lee, H., Grebel, E. K., & Hodge, P. W. 2003, *A&A*, 401, 141
- Lee, H., McCall, M. L., Kingsburgh, R. L., Ross, R., & Stevenson, C. C. 2003, *AJ*, 125, 146
- Lee, J. C., et al. 2009, *ApJ*, 706, 599
- Leger, A., & Puget, J. L. 1984, *A&A*, 137, L5
- Leroy, A., Bolatto, A. D., Simon, J. D., & Blitz, L. 2005, *ApJ*, 625, 763
- Mateo, M. L. 1998, *ARA&A*, 36, 435
- O’Halloran, B., Satyapal, S., & Dudik, R. P. 2006, *ApJ*, 641, 795
- Ricks, A. M., Douberly, G. E., & Duncan, M. A. 2009, *ApJ*, 702, 301
- Rosenberg, J. L., Ashby, M. L. N., Salzer, J. J., & Huang, J.-S. 2006, *ApJ*, 636, 742
- Sanders, D. B., & Mirabel, I. F. 1996, *ARA&A*, 34, 749
- Sanders, D. B., Soifer, B. T., Elias, J. H., Madore, B. F., Matthews, K., Neugebauer, G., & Scoville, N. Z. 1988, *ApJ*, 325, 74
- Skrutskie, M. F., et al. 2006, *AJ*, 131, 1163
- Smith, J. D. T., et al. 2007b, *PASP*, 119, 1133

- Smith, J. D. T., et al. 2007a, ApJ, 656, 770
- Taylor, C. L., Kobulnicky, H. A., & Skillman, E. D. 1998, AJ, 116, 2746
- Tenorio-Tagle, G., & Bodenheimer, P. 1988, ARA&A, 26, 145
- Tielens, A. G. G. M. 2008, ARA&A, 46, 289
- Webster, B. L., & Smith, M. G. 1983, MNRAS, 204, 743
- Wu, R., Hogg, D. W., & Moustakas, J. 2010, ApJ, submitted (arxiv/0907.1783)

Table 1. Galaxy Sample Properties

Target	Type ^a	M_B (mag)	Distance ^b (Mpc)	$12+\log(\text{O}/\text{H})^c$ (dex)	Mass ($10^6 M_\odot$)	Current Star Formation Rate ($M_\odot \text{ yr}^{-1}$)	Diffuse 8 μm Flux Density ^d (Jy)
NGC 55	IrrIV	-17.5	2.17	8.4 ± 0.1	15600	5.40×10^{-1}	1.4
NGC 3109	IrrIV-V	-15.2	1.34	7.74 ± 0.33	6550	3.98×10^{-2}	0.06
IC 5152	dIrr	-14.5	1.97	7.92 ± 0.07	400	3.47×10^{-2}	0.16

^aType, M_B , and mass (calculated from central or rotational velocity, as available) taken from Mateo (1998)

^bDistance and SFR taken from Lee et al. (2009). SFR based on GALEX FUV integrated photometry and corrected for extinction based on $A_{FUV} = 7.9E(B - V)$, except for NGC 3109, where UV attenuation was unavailable, and $H\alpha$ attenuation ($A_{H\alpha} = 2.5E(B - V)$, scaled to a factor of 1.8, was used instead

^cMetallicities taken from Webster & Smith (1983) for NGC 55, Lee et al. (2003a) for IC 5152, and Lee et al. (2003b) for NGC 3109.

^dDiffuse 8 μm flux density taken from Jackson et al. (2006)

Table 2. Global Feature Radiances From PAHFIT^a

Wavelength	NGC 55	NGC 3109	IC 5152
6.2 μm PAH	76.5 ± 0.9	4.5 ± 0.6	12.0 ± 0.7
7.7 μm PAH	226.1 ± 3.6	12.8 ± 1.9	26.3 ± 2.7
8.6 μm PAH	43.0 ± 0.6	0.9 ± 0.4	8.4 ± 0.3
[S IV] 10.5 μm	7.0 ± 0.1	0.2 ± 0.1	0.5 ± 0.1
11.3 μm PAH	73.4 ± 0.9	1.9 ± 0.2	14.3 ± 0.5
12.6 μm PAH	29.7 ± 0.4	0.9 ± 0.1	3.2 ± 0.3
[Ne II] 12.8 μm	8.3 ± 0.1	0.5 ± 0.1	1.4 ± 0.1

^aUnits of $10^{-9} \text{ W m}^{-2} \text{ sr}^{-1}$.

Table 3. Global PAH Ratios^a

Target	(6.2 μm)/(11.3 μm)	(7.7 μm)/(11.3 μm)	(8.6 μm)/(11.3 μm)	(7.7 μm)/(6.2 μm)	(8.6 μm)/(6.2 μm)
NGC 55	1.04 ± 0.02	3.07 ± 0.06	0.59 ± 0.01	2.95 ± 0.06	0.56 ± 0.01
NGC 3109	2.39 ± 0.38	6.72 ± 1.14	0.46 ± 0.19	2.81 ± 0.56	0.19 ± 0.08
IC 5152	0.84 ± 0.06	1.84 ± 0.20	0.58 ± 0.03	2.20 ± 0.25	0.70 ± 0.05

^aValues are ratios of radiances measured in $\text{W m}^{-2} \text{sr}^{-1}$.

Table 4. Spectral Extraction Wavelength Regions^a

Target	6.2 μm	7.7 μm	8.6 μm	Broad 8 μm	11.3 μm	[Ne II] 12.8 μm
NGC 55	5.986-6.513	7.536-7.882	8.403-8.838	7.288-8.900	10.949-11.694	12.625-12.998
NGC 3109	6.141-6.358	7.443-7.782	8.217-8.900	7.288-8.900	10.763-11.570	12.688-12.936
IC 5152	6.110-6.420	7.474-7.882	8.403-8.838	7.288-8.900	11.073-11.446	12.688-12.998

^aSpectral extraction regions are given in units of μm .

Table 5. PAH/PAH Ratios for NGC 55 Extraction Regions^a

Region	(6.2 μm)/(11.3 μm)	(7.7 μm)/(11.3 μm)	(8.6 μm)/(11.3 μm)	(7.7 μm)/(6.2 μm)	(8.6 μm)/(6.2 μm)
Region 1	0.93 ± 0.07	2.73 ± 0.29	0.53 ± 0.04	2.92 ± 0.36	0.56 ± 0.06
Region 2	1.15 ± 0.16	2.41 ± 0.50	0.34 ± 0.08	2.10 ± 0.51	0.29 ± 0.08
Region 3	1.01 ± 0.07	2.97 ± 0.21	0.45 ± 0.04	2.93 ± 0.27	0.44 ± 0.05
Region 4	1.14 ± 0.08	3.28 ± 0.27	0.55 ± 0.04	2.87 ± 0.29	0.48 ± 0.04
Region 5	1.04 ± 0.05	2.88 ± 0.15	0.56 ± 0.03	2.78 ± 0.14	0.54 ± 0.02
Region 6	1.10 ± 0.05	3.29 ± 0.14	0.59 ± 0.03	2.99 ± 0.12	0.54 ± 0.03
Region 7	1.02 ± 0.04	3.07 ± 0.11	0.51 ± 0.02	3.01 ± 0.16	0.50 ± 0.03
Region 8	1.10 ± 0.05	3.28 ± 0.16	0.57 ± 0.03	2.98 ± 0.12	0.52 ± 0.02
Region 9	1.32 ± 0.04	3.88 ± 0.11	0.63 ± 0.02	2.94 ± 0.09	0.47 ± 0.02
Region 10	1.12 ± 0.06	2.88 ± 0.17	0.53 ± 0.03	2.57 ± 0.20	0.48 ± 0.04
Region 11	1.11 ± 0.05	3.58 ± 0.15	0.60 ± 0.03	3.23 ± 0.12	0.55 ± 0.03
Region 12	1.15 ± 0.04	3.33 ± 0.12	0.57 ± 0.02	2.91 ± 0.13	0.50 ± 0.02
Region 13	1.14 ± 0.03	3.51 ± 0.12	0.57 ± 0.02	3.09 ± 0.13	0.50 ± 0.02
Region 14	1.12 ± 0.05	3.56 ± 0.17	0.62 ± 0.03	3.17 ± 0.15	0.55 ± 0.03
Region 15	1.11 ± 0.08	3.20 ± 0.22	0.49 ± 0.04	2.88 ± 0.19	0.45 ± 0.04
Region 16	1.06 ± 0.14	2.31 ± 0.19	0.37 ± 0.07	2.17 ± 0.32	0.35 ± 0.08
Region 17	1.13 ± 0.05	3.20 ± 0.20	0.59 ± 0.04	2.82 ± 0.18	0.52 ± 0.03
Region 18	1.23 ± 0.12	2.66 ± 0.39	0.47 ± 0.07	2.16 ± 0.37	0.38 ± 0.06
Region 19	1.27 ± 0.11	2.66 ± 0.39	0.47 ± 0.06	2.10 ± 0.32	0.37 ± 0.05
Weighted Mean	1.13 ± 0.01	3.27 ± 0.04	0.56 ± 0.01	2.94 ± 0.04	0.50 ± 0.01
Standard Deviation	0.09	0.42	0.08	0.37	0.08

^aValues are ratios of radiances measured in of $\text{W m}^{-2} \text{ sr}^{-1}$.

Table 6. Selected Ratios for NGC 55 Extraction Regions^a

Region	[Ne II]/(11.3 μm)	[Ne II]/(8.6 μm)	(MIPS 24 μm)/(11.3 μm)	(MIPS 24 μm)/(8.6 μm)
Region 1	$0.03 \pm 0.01^{\text{b}}$	0.05 ± 0.01	59.7 ± 1.48	113 ± 9.13
Region 2	0.06 ± 0.01	0.16 ± 0.05	191 ± 8.08	563 ± 131
Region 3	0.10 ± 0.01	0.23 ± 0.02	246 ± 4.80	548 ± 44.4
Region 4	0.10 ± 0.01	0.18 ± 0.02	110 ± 2.26	198 ± 13.1
Region 5	0.11 ± 0.01	0.19 ± 0.01	97.6 ± 3.25	174 ± 6.09
Region 6	0.10 ± 0.01	0.17 ± 0.01	101 ± 3.45	170 ± 6.08
Region 7	0.05 ± 0.01	0.10 ± 0.01	66.2 ± 0.67	129 ± 4.73
Region 8	0.07 ± 0.01	0.12 ± 0.01	95.1 ± 3.56	166 ± 5.98
Region 9	0.15 ± 0.01	0.23 ± 0.01	333 ± 5.25	530 ± 14.2
Region 10	0.04 ± 0.01	0.08 ± 0.01	905 ± 15.01	1700 ± 105
Region 11	0.08 ± 0.01	0.13 ± 0.01	101 ± 3.45	168 ± 6.38
Region 12	0.06 ± 0.01	0.11 ± 0.01	114 ± 1.38	199 ± 7.85
Region 13	0.09 ± 0.01	0.15 ± 0.01	106 ± 1.07	185 ± 5.82
Region 14	0.10 ± 0.01	0.16 ± 0.01	178 ± 5.75	287 ± 11.5
Region 15	0.09 ± 0.01	0.17 ± 0.01	157 ± 8.09	317 ± 20.8
Region 16	0.03 ± 0.01	0.08 ± 0.03	689 ± 25.51	1870 ± 369
Region 17	0.17 ± 0.01	0.29 ± 0.02	221 ± 7.01	377 ± 19.6
Region 18	0.05 ± 0.01	0.11 ± 0.03	521 ± 16.51	1100 ± 152
Region 19	0.17 ± 0.01	0.36 ± 0.05	701 ± 34.90	1490 ± 175
Weighted Mean	0.08 ± 0.01	0.15 ± 0.01	89.5 ± 0.46	181 ± 2.07
Standard Deviation	0.04	0.08	252	564

^aValues are ratios of radiances measured in $\text{W m}^{-2} \text{sr}^{-1}$.

^bFor some regions, errors were below .005. In these cases, the error was rounded up to 0.01.

Table 7. PAH/PAH Ratios for NGC 3109 Extraction Regions^a

Region	(6.2 μm)/(11.3 μm)	(7.7 μm)/(11.3 μm)	(8.6 μm)/(11.3 μm)	(7.7 μm)/(6.2 μm)	(8.6 μm)/(6.2 μm)
Region 1	2.45 ± 1.30	6.91 ± 4.50	0.49 ± 0.66	2.82 ± 1.93	0.20 ± 0.27
Region 2	3.09 ± 1.60	9.32 ± 4.97	0.76 ± 0.79	3.02 ± 1.50	0.25 ± 0.25
Region 3	1.55 ± 0.41	5.26 ± 1.11	0.32 ± 0.24	3.40 ± 0.98	0.21 ± 0.16
Region 4	4.01 ± 1.42	10.23 ± 3.45	0.98 ± 0.48	2.55 ± 0.89	0.24 ± 0.12
Weighted Mean	1.86 ± 0.37	5.93 ± 1.00	0.47 ± 0.19	2.94 ± 0.58	0.23 ± 0.09
Standard Deviation	1.04	2.26	0.29	0.36	0.02

^aValues are ratios of radiances measured in $\text{W m}^{-2} \text{sr}^{-1}$.

Table 8. Selected Ratios for NGC 3109 Extraction Regions^a

Region	[Ne II]/(11.3 μm)	[Ne II]/(8.6 μm)	(MIPS 24 μm)/(11.3 μm)	(MIPS 24 μm)/(8.6 μm)
Region 1	0.02 ± 0.02	0.06 ± 0.10	2420 ± 1420	7560 ± 2550
Region 2	0.14 ± 0.10	0.18 ± 0.20	635 ± 609	808 ± 1850
Region 3	0.25 ± 0.05	1.25 ± 0.03	269 ± 42.4	1330 ± 1950
Region 4	0.11 ± 0.06	0.09 ± 0.06	617 ± 257	533 ± 330
Weighted Mean	0.06 ± 0.02	0.09 ± 0.05	281 ± 41.7	564 ± 320
Standard Deviation	0.10	0.57	972	3350

^aValues are ratios of radiances measured in of $\text{W m}^{-2} \text{sr}^{-1}$.

Table 9. PAH/PAH Ratios for IC 5152 Extraction Regions^a

Region	(6.2 μm)/(11.3 μm)	(7.7 μm)/(11.3 μm)	(8.6 μm)/(11.3 μm)	(7.7 μm)/(6.2 μm)	(8.6 μm)/(6.2 μm)
Region 1	1.18 ± 0.47	2.63 ± 1.58	0.36 ± 0.26	2.22 ± 1.50	0.30 ± 0.24
Region 2	1.25 ± 0.14	3.17 ± 0.53	0.58 ± 0.10	2.52 ± 0.48	0.46 ± 0.09
Region 3	0.96 ± 0.10	3.04 ± 0.39	0.41 ± 0.06	3.18 ± 0.50	0.43 ± 0.07
Region 4	1.01 ± 0.17	3.08 ± 0.46	0.55 ± 0.09	3.04 ± 0.65	0.54 ± 0.12
Region 5	0.80 ± 0.20	3.89 ± 0.31	0.21 ± 0.11	4.87 ± 1.23	0.26 ± 0.15
Region 6	0.83 ± 0.33	1.80 ± 0.44	0.22 ± 0.15	2.18 ± 0.84	0.27 ± 0.20
Region 7	0.83 ± 0.11	2.41 ± 0.32	0.41 ± 0.06	2.89 ± 0.54	0.49 ± 0.10
Region 8	0.83 ± 0.17	2.39 ± 0.52	0.44 ± 0.11	2.89 ± 0.58	0.53 ± 0.12
Region 9	0.75 ± 0.16	2.15 ± 0.43	0.46 ± 0.08	2.85 ± 0.81	0.61 ± 0.16
Region 10	1.08 ± 0.17	3.17 ± 0.59	0.64 ± 0.10	2.93 ± 0.53	0.59 ± 0.09
Weighted Mean	0.95 ± 0.05	2.85 ± 0.14	0.45 ± 0.03	2.89 ± 0.20	0.48 ± 0.04
Standard Deviation	0.17	0.61	0.14	0.75	0.13

^aValues are ratios of radiances measured in $\text{W m}^{-2} \text{sr}^{-1}$.

Table 10. Selected Ratios for IC 5152 Extraction Regions^a

Region	[Ne II]/(11.3 μm)	[Ne II]/(8.6 μm)	(MIPS 24 μm)/(11.3 μm)	(MIPS 24 μm)/(8.6 μm)
Region 1	0.13 ± 0.05	0.36 ± 0.28	71.6 ± 17.7	201.59 ± 172
Region 2	0.08 ± 0.01	0.14 ± 0.03	48.2 ± 2.07	83.28 ± 13.3
Region 3	0.07 ± 0.01	0.17 ± 0.03	53.2 ± 1.59	128.15 ± 17.6
Region 4	0.07 ± 0.01	0.13 ± 0.03	50.8 ± 2.10	91.87 ± 13.6
Region 5	0.08 ± 0.03	0.38 ± 0.23	43.2 ± 2.43	205.54 ± 105
Region 6	0.06 ± 0.03	0.29 ± 0.23	78.9 ± 14.4	354.78 ± 236
Region 7	0.10 ± 0.01	0.25 ± 0.05	41.7 ± 1.42	102.57 ± 15.1
Region 8	0.06 ± 0.01	0.13 ± 0.03	39.0 ± 6.04	89.01 ± 17.6
Region 9	0.04 ± 0.02	0.10 ± 0.04	41.7 ± 1.97	91.13 ± 15.7
Region 10	0.13 ± 0.02	0.20 ± 0.03	140 ± 15.8	218.37 ± 24.5
Weighted Mean	0.08 ± 0.01	0.16 ± 0.01	46.6 ± 0.74	104 ± 6.00
Standard Deviation	0.03	0.10	30.7	88.0

^aValues are ratios of radiances measured in $\text{W m}^{-2} \text{ sr}^{-1}$.

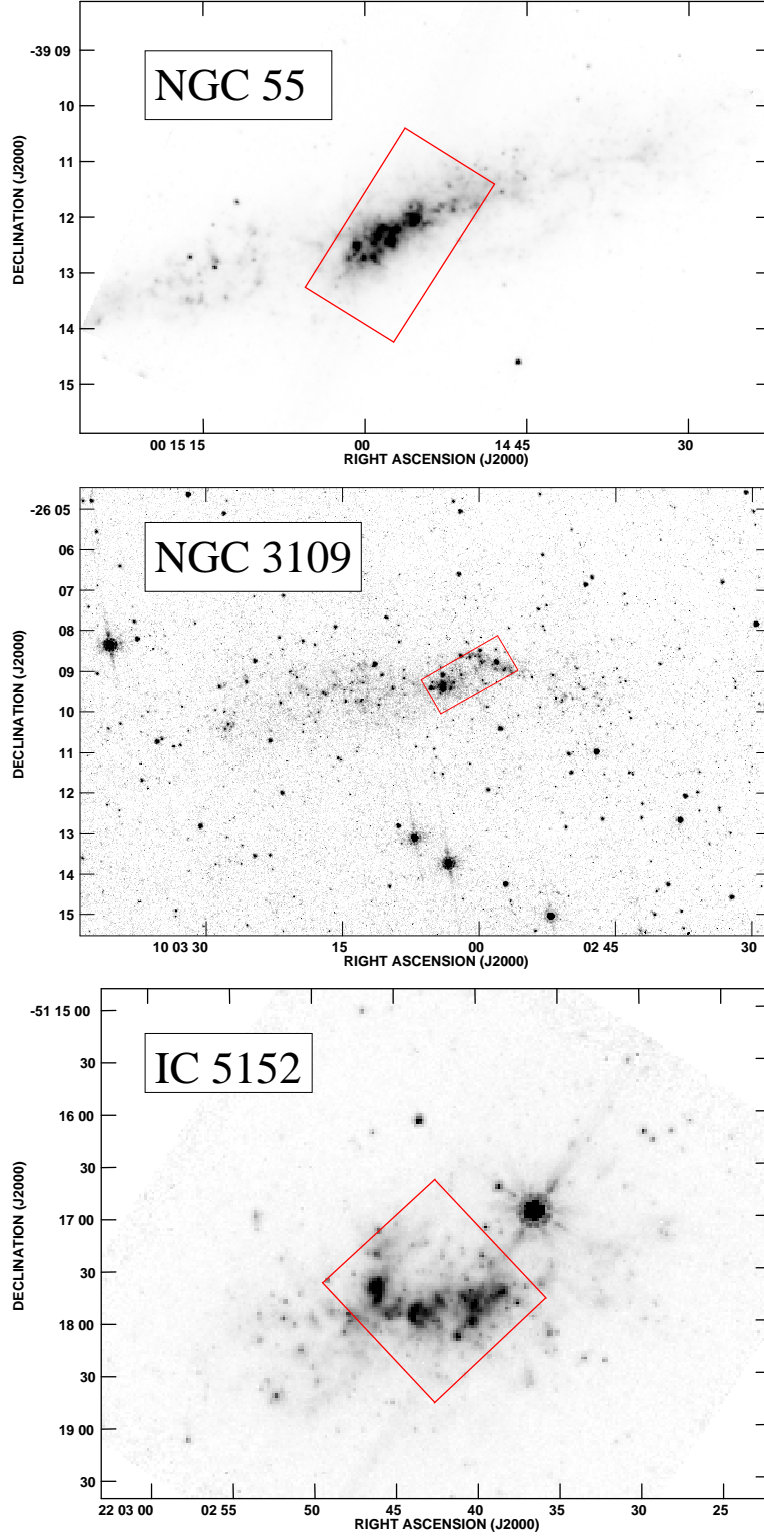


Fig. 1.— IRAC 8 μm images are shown for each of the target galaxies with the region observed by IRS boxed in red. Images have arbitrary scaling to highlight features. Galactic foreground stars are prominent in NGC 3109 and IC 5152 (see in particular the object near IC 5152, $\alpha \approx 22:02:36$, $\delta \approx -51:16:55$).

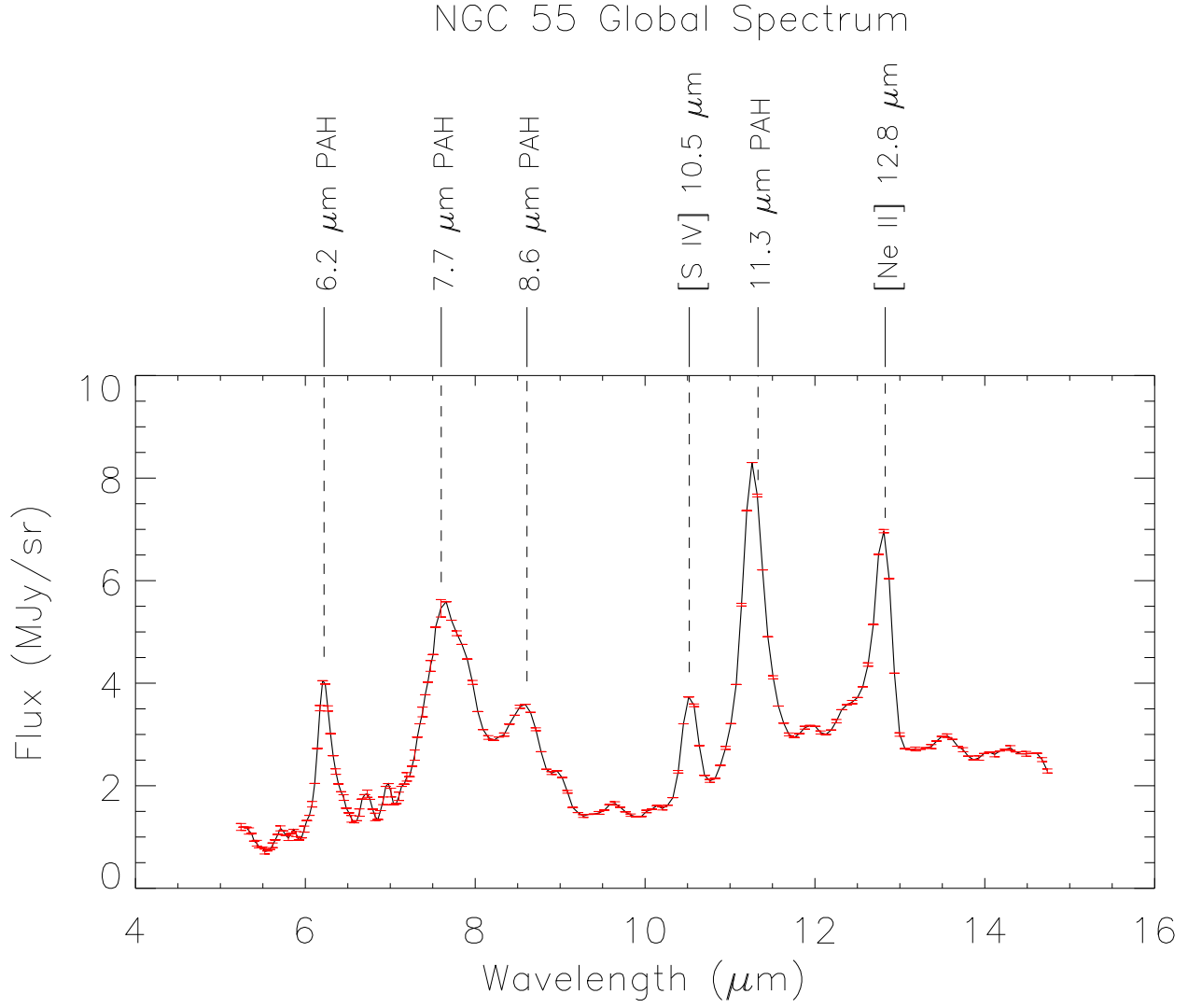


Fig. 2.— Global IRS spectrum for NGC 55, with prominent emission lines and PAH features labeled. Errors are shown in red, and are largest in the region of overlap between the SL1 and SL2 slits, between 7.4 μm and 7.7 μm.

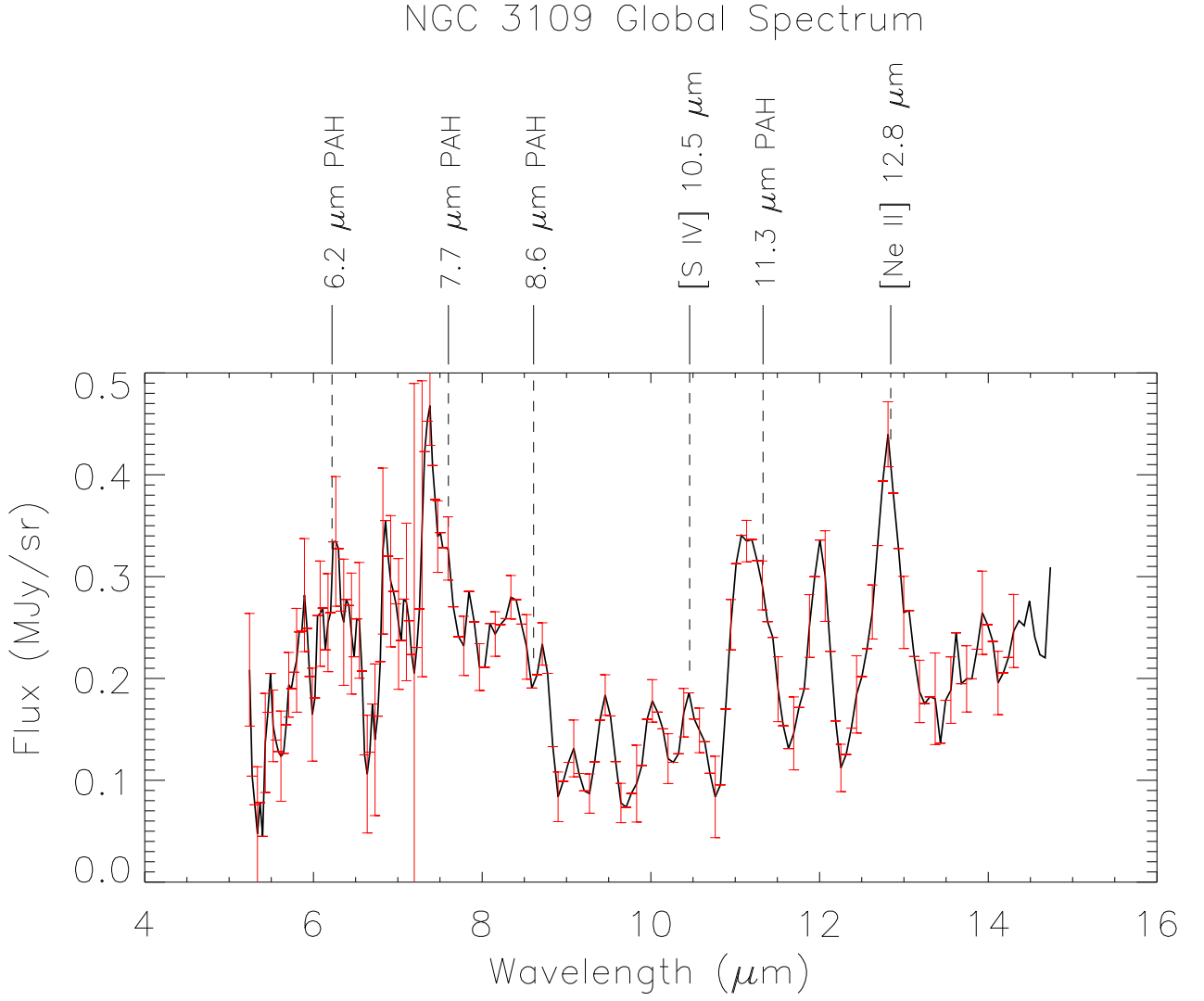


Fig. 3.— Global IRS spectrum for NGC 3109, with prominent emission lines and PAH features labeled. Errors are shown in red, and are largest in the region of overlap between the SL1 and SL2 slits, between 7.4 μm and 7.7 μm .

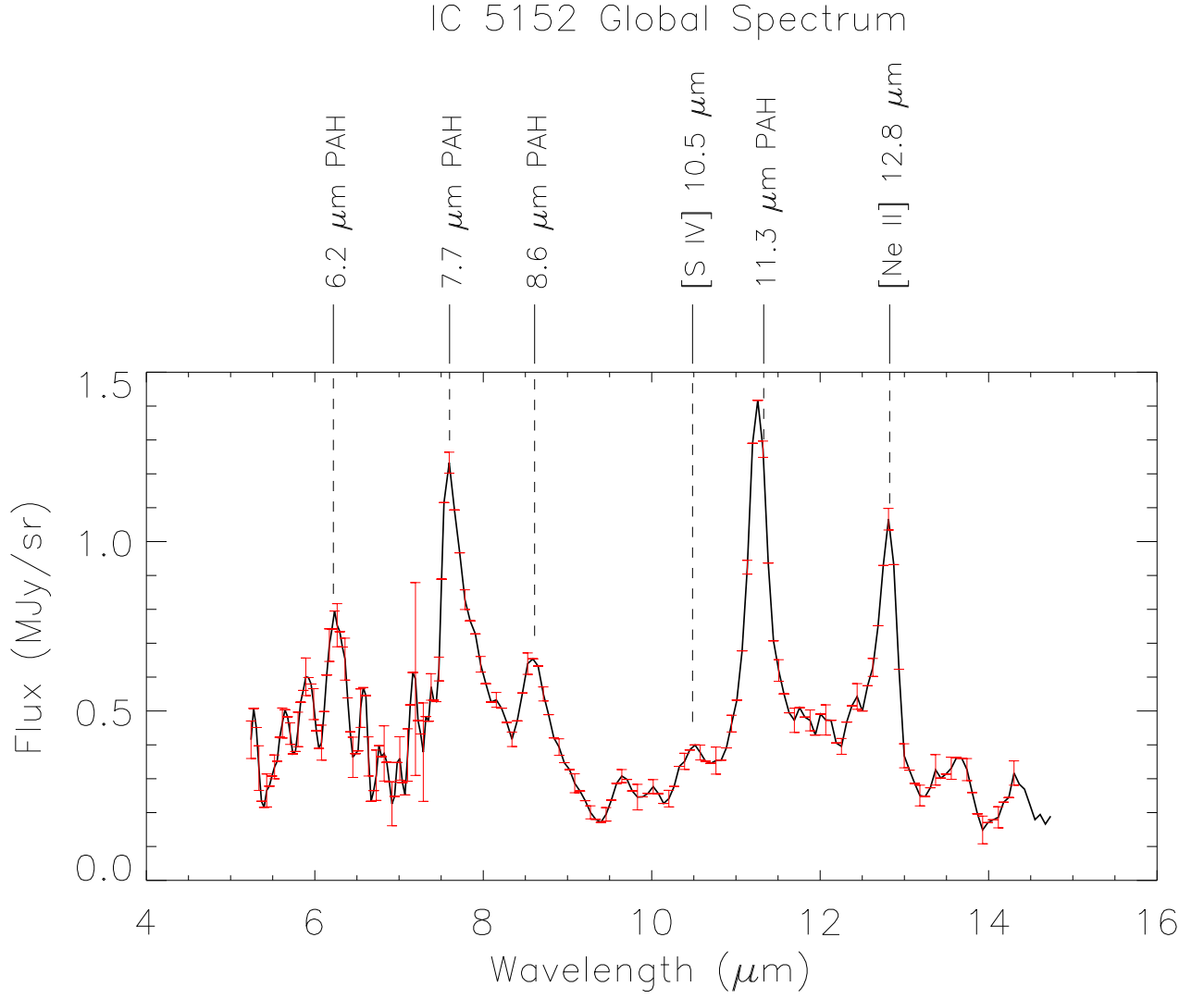


Fig. 4.— Global IRS spectrum for IC 5152, with prominent emission lines and PAH features labeled. Errors are shown in red, and are largest in the region of overlap between the SL1 and SL2 slits, between 7.4 μm and 7.7 μm.

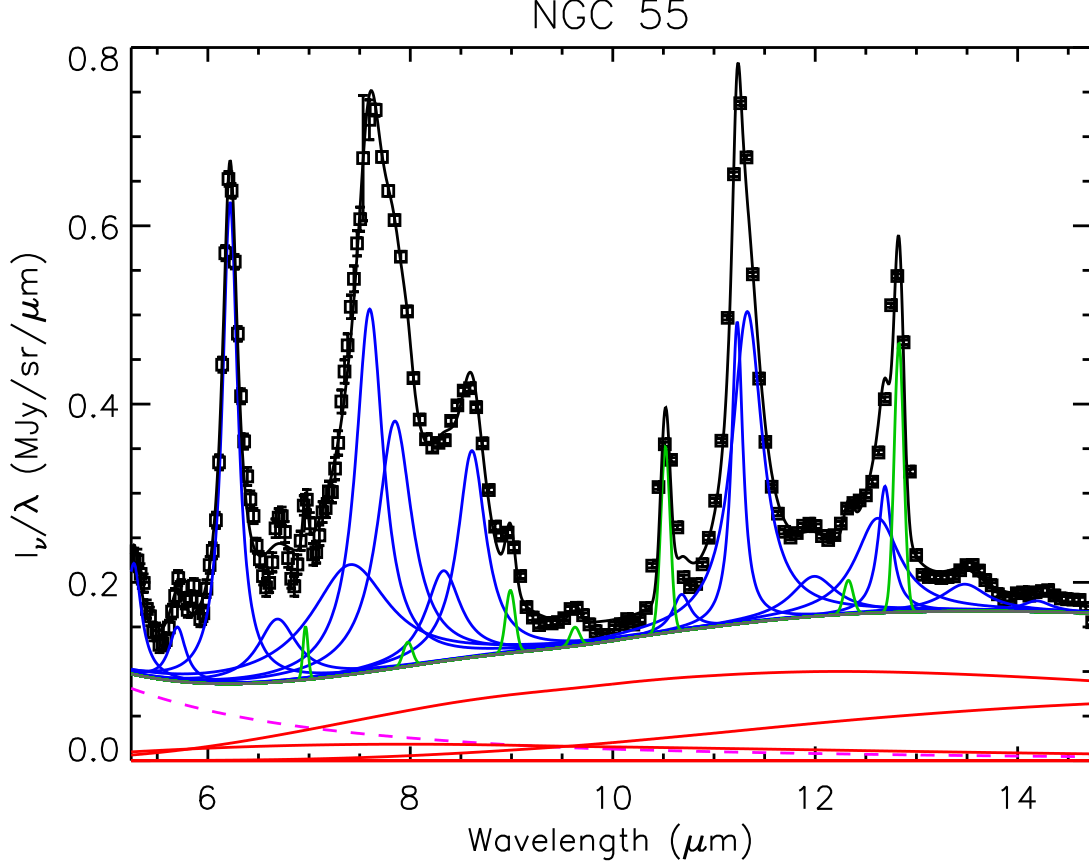


Fig. 5.— Decomposed global IRS spectrum for NGC 55 produced by PAHFIT. The red lines represent thermal dust continuum components at various temperatures, the dashed magenta line the stellar continuum, the gray line the total (dust + stellar) continuum. The blue line represents the PAH features, the green line the unresolved atomic and molecular spectral lines, and the black line the full fitted model.

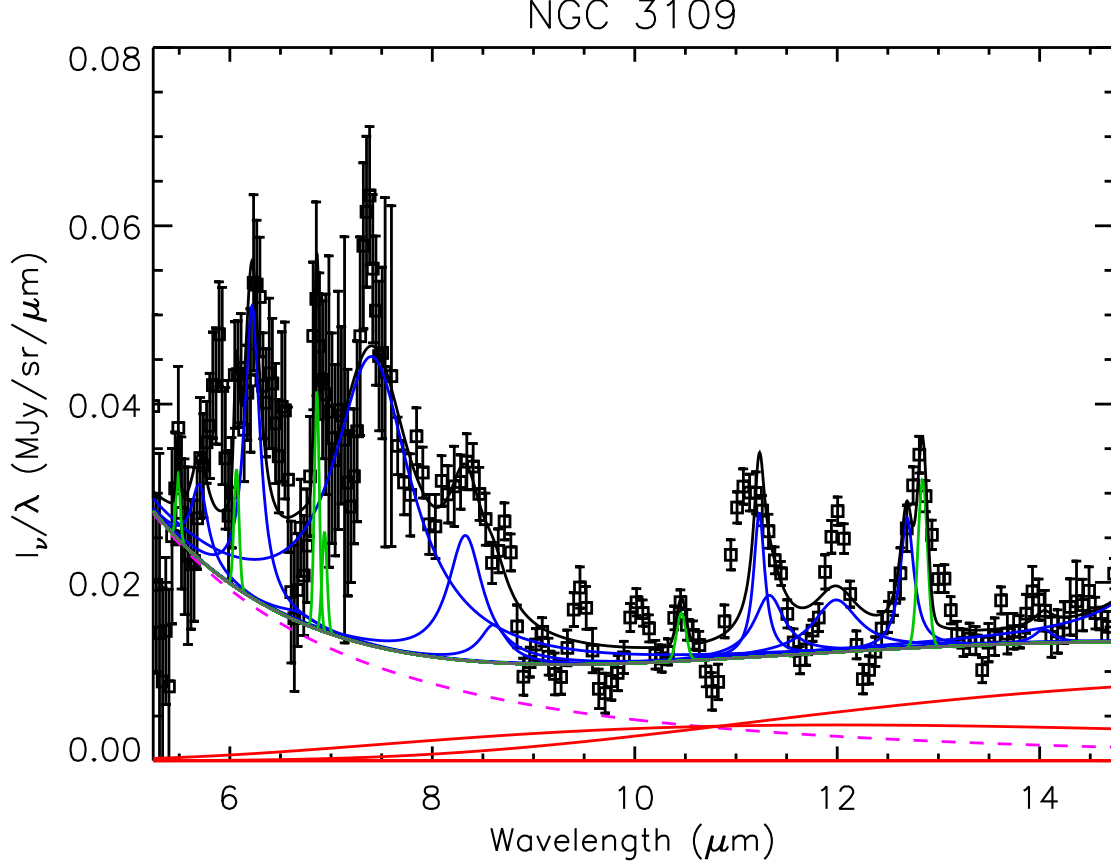


Fig. 6.— Decomposed global IRS spectrum for NGC 3109 produced by PAHFIT. The red lines represent thermal dust continuum components at various temperatures, the dashed magenta line the stellar continuum, the gray line the total (dust + stellar) continuum. The blue line represents the PAH features, the green line the unresolved atomic and molecular spectral lines, and the black line the full fitted model.

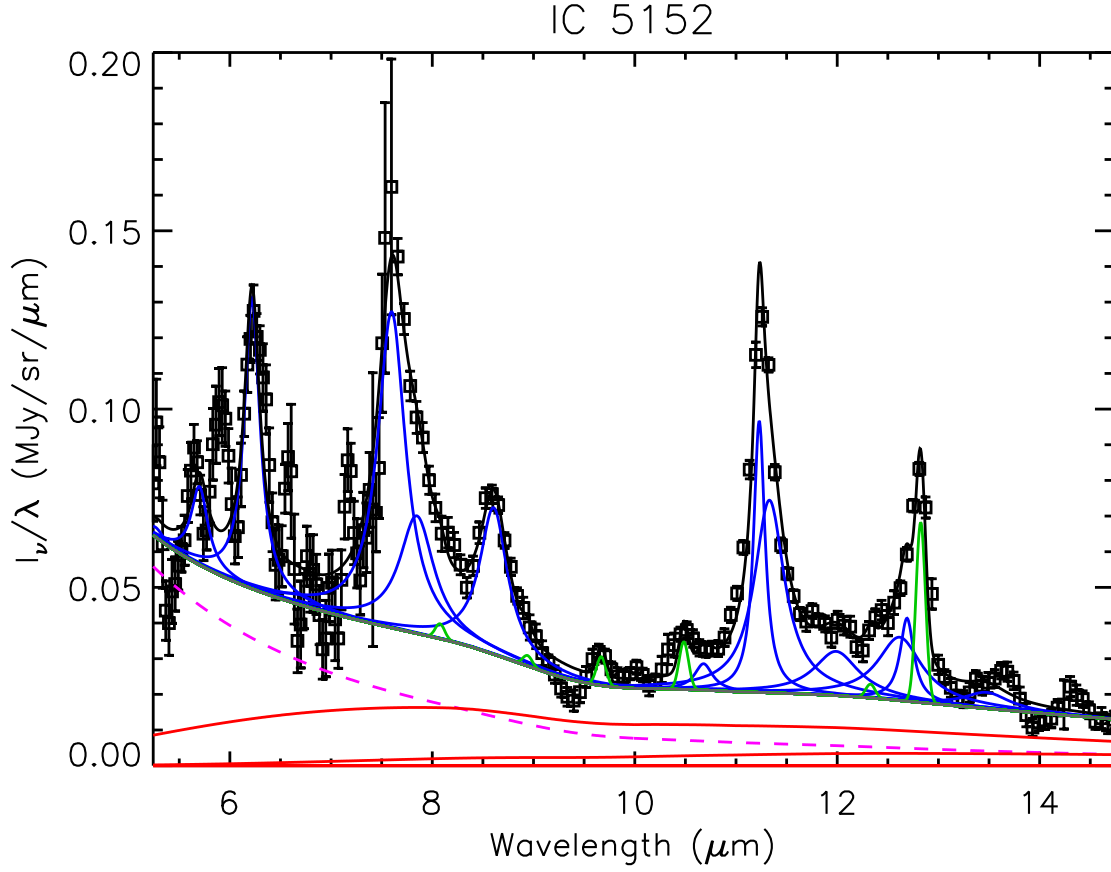


Fig. 7.— Decomposed global IRS spectrum for IC 5152 produced by PAHFIT. The red lines represent thermal dust continuum components at various temperatures, the dashed magenta line the stellar continuum, the gray line the total (dust + stellar) continuum. The blue line represents the PAH features, the green line the unresolved atomic and molecular spectral lines, and the black line the full fitted model.

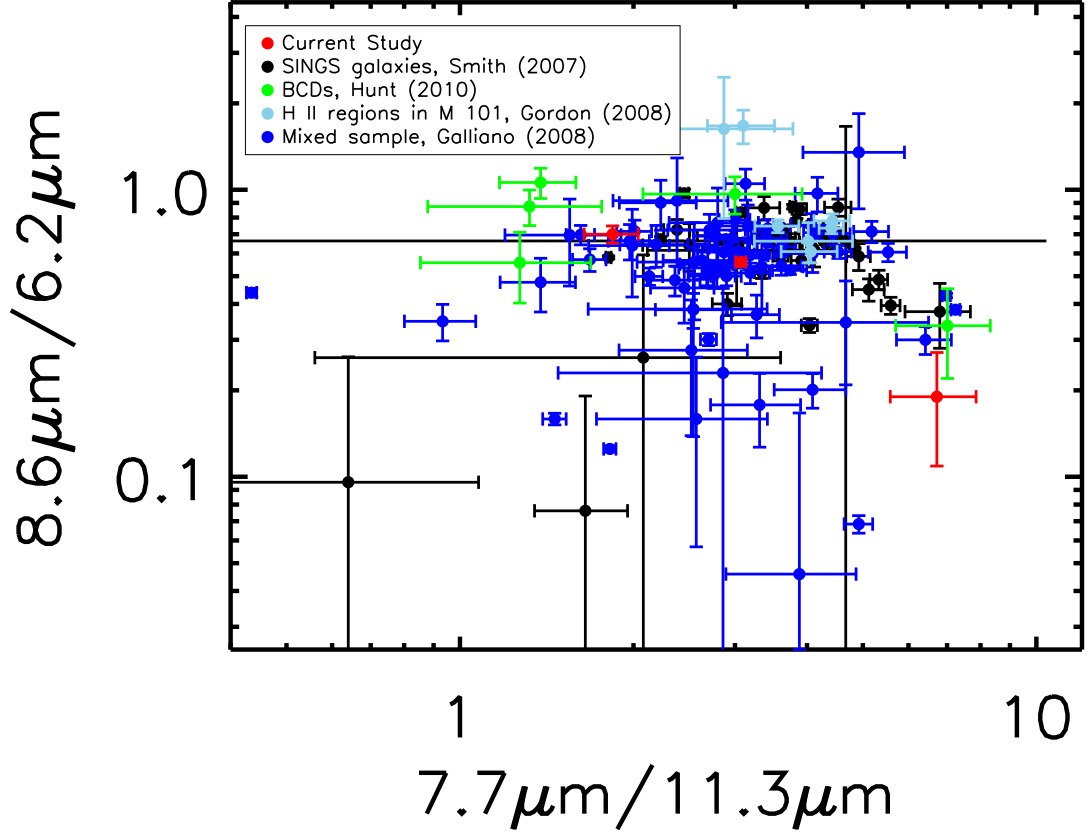


Fig. 8.— Global comparison of PAH/PAH radiance ratios for individual galaxies and selected massive star formation regions. The four systems with the lowest $(8.6 \mu\text{m})/(6.2 \mu\text{m})$ ratios are NGC 4725, NGC 1291, IRAS 23128-5919, and NGC 253, in order of increasing $(7.7 \mu\text{m})/(11.3 \mu\text{m})$ ratio. This plot is designed to show contributions from larger PAH molecules increasing up the y axis, and contributions from ionized PAH molecules increasing along the x axis. The galaxies from our sample fall within the range established by the larger samples.

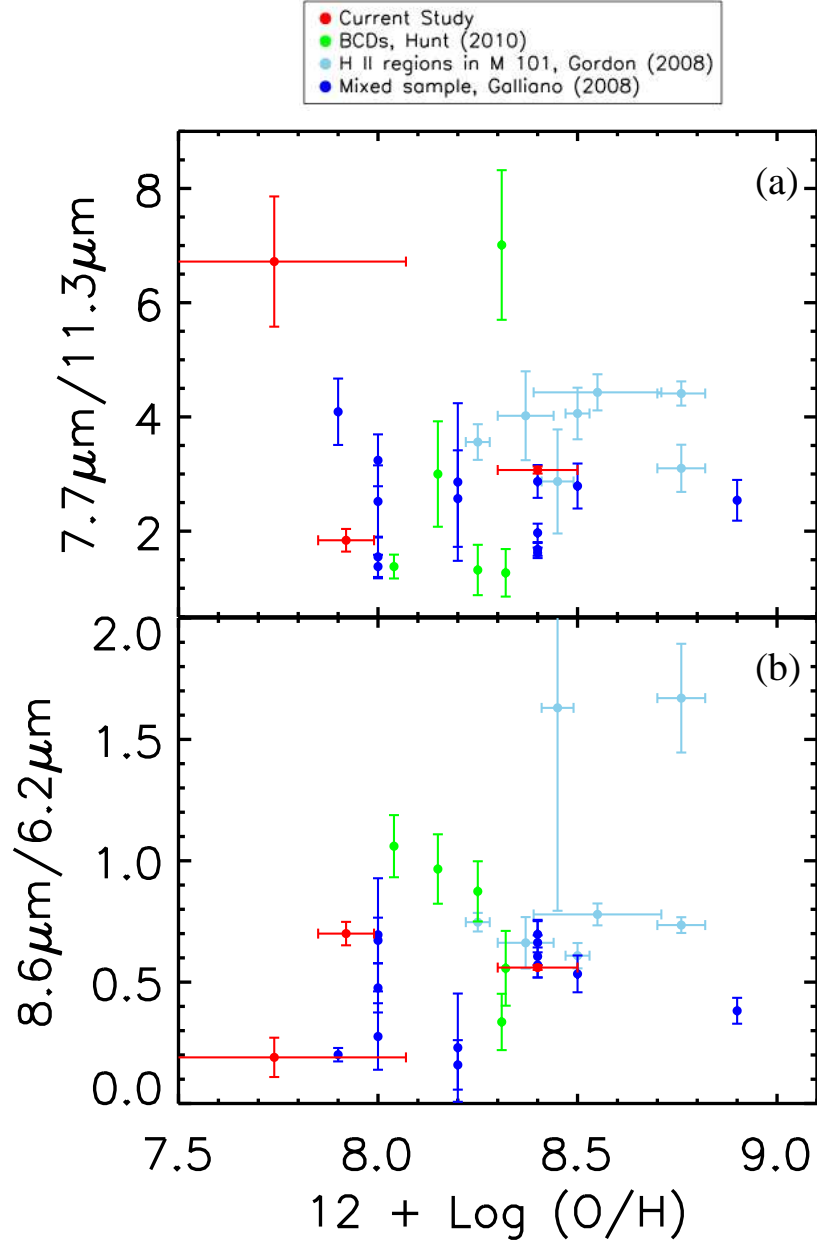


Fig. 9.— Comparison of PAH/PAH radiance ratios with gas-phase oxygen abundances in dwarf galaxies and in individual H II regions in M 101. No uncertainties in metallicity were available for the Hunt et al. (2010) or Galliano et al. (2008) data. Only very weak trends with metallicity are apparent from this plot.

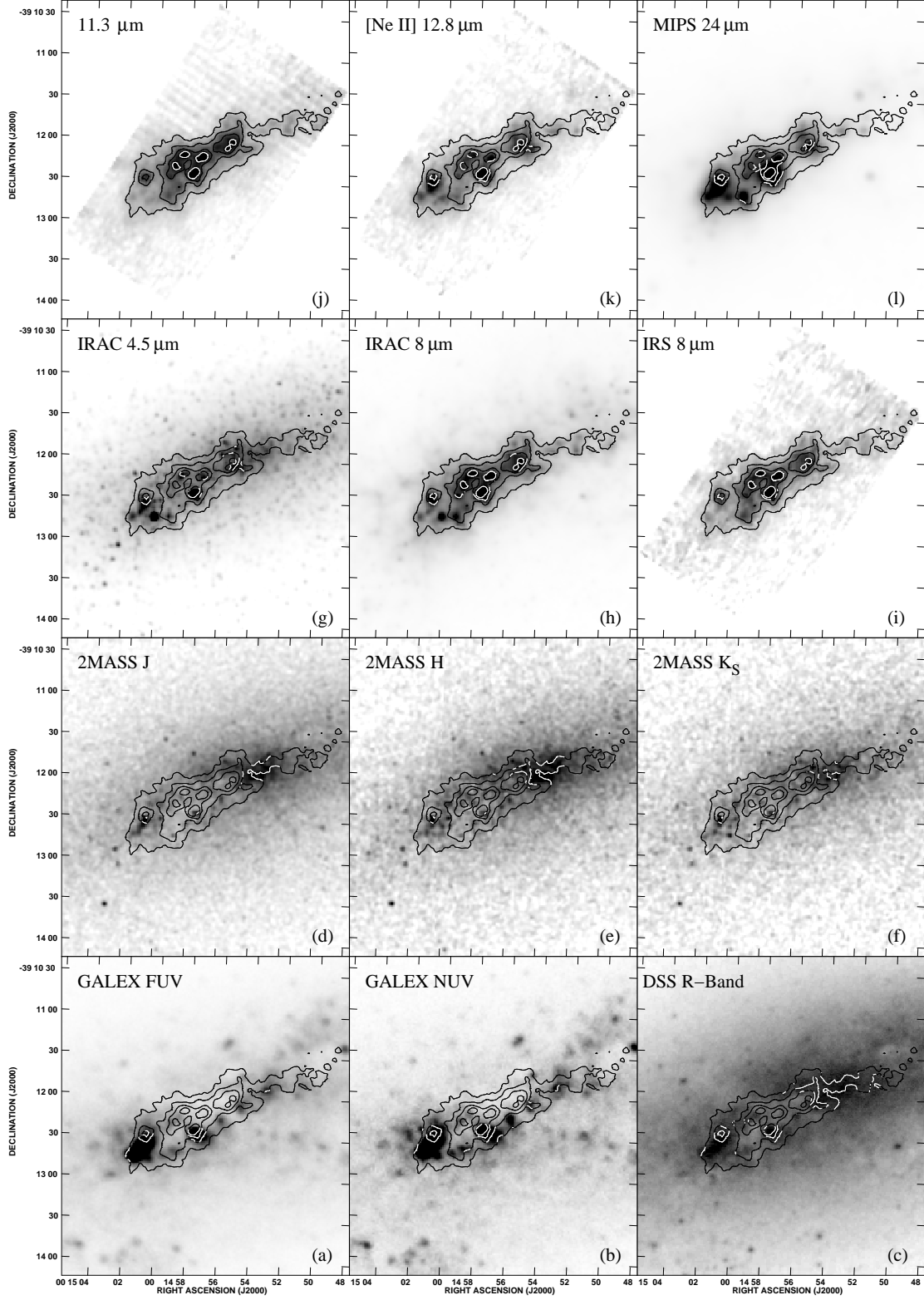


Fig. 10.— Multiwavelength images of the region of NGC 55 covered by the IRS spectral map, ordered by increasing wavelength from (a) to (l) as labeled. Contours of $11.3 \mu\text{m}$ surface brightness are overlaid in each panel at the $1.5, 3, 4.5$ and 6 MJy sr^{-1} levels.

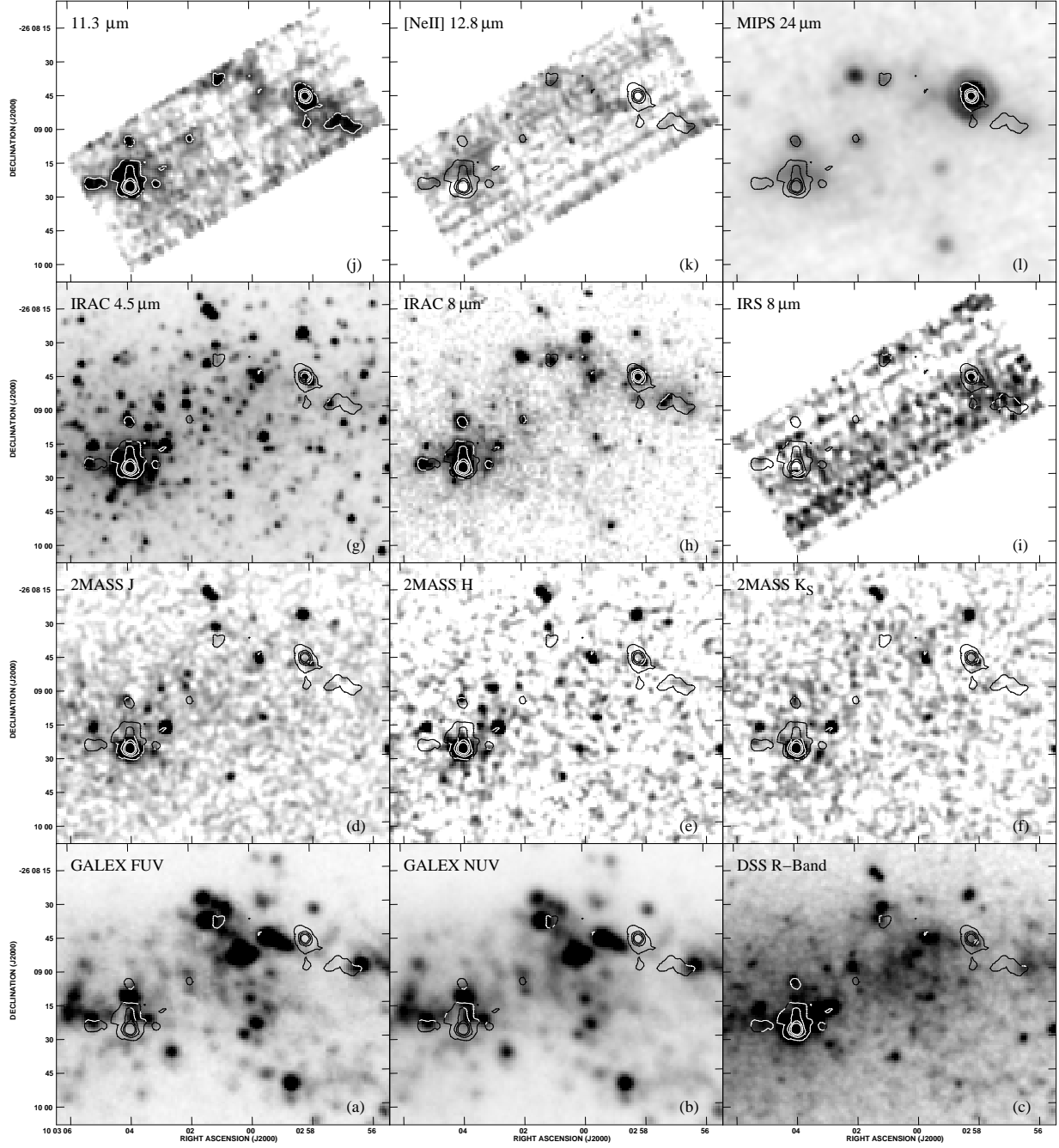


Fig. 11.— Multiwavelength images of the region of NGC 3109 covered by the IRS spectral map, ordered by increasing wavelength from (a) to (l) as labeled. Contours of 11.3 μm surface brightness are overlaid in each panel at the 0.5, 1.0, 1.5 and 2.0 MJy sr⁻¹ levels.

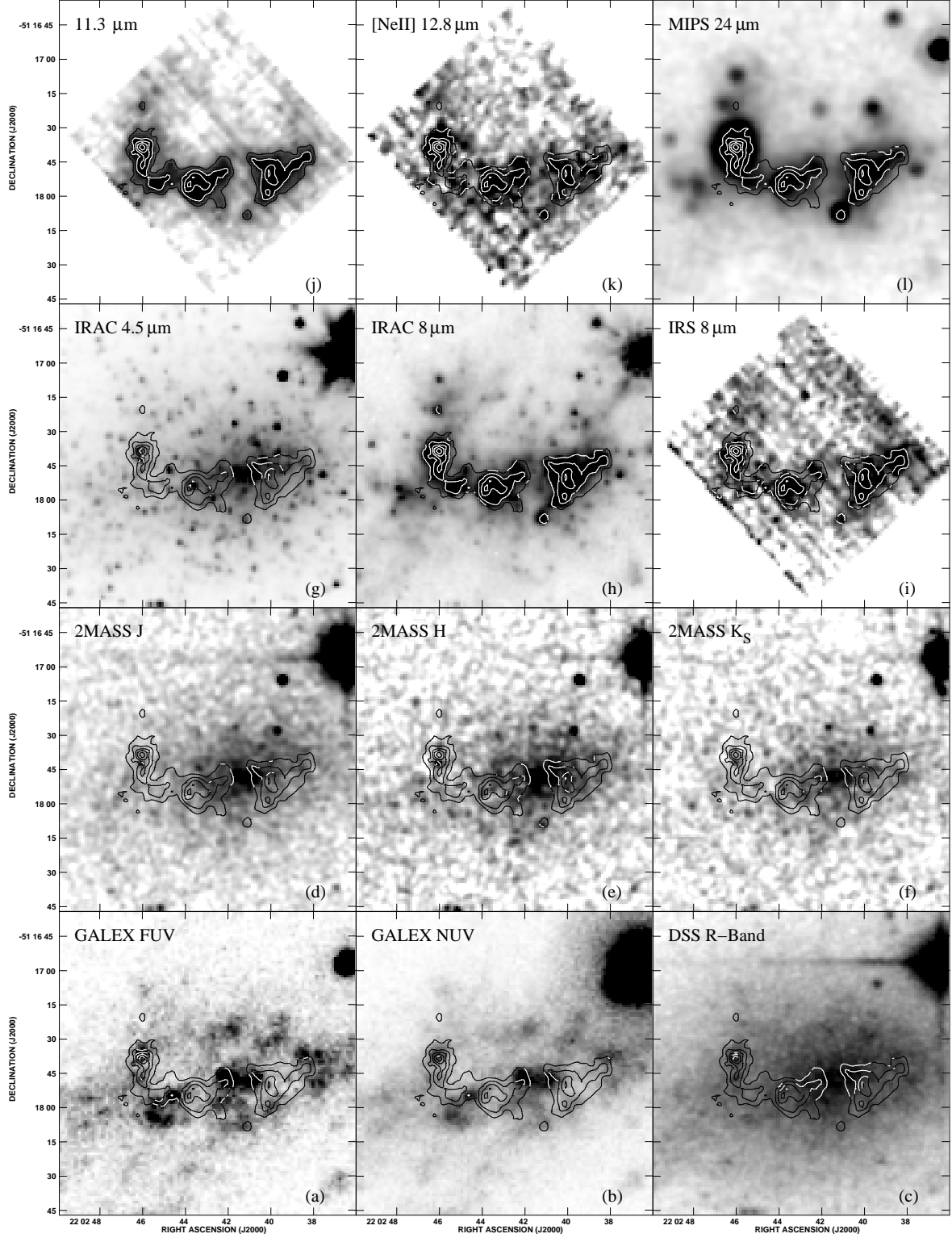


Fig. 12.— Multiwavelength images of the region of IC 5152 covered by the IRS spectral map, ordered by increasing wavelength from (a) to (l) as labeled. Contours of 11.3 μm surface brightness are overlaid in each panel at the 1.0, 1.5, 2.0, 2.5 and 3.0 MJy sr⁻¹ levels. The extremely luminous source in the upper right is a Galactic foreground star.

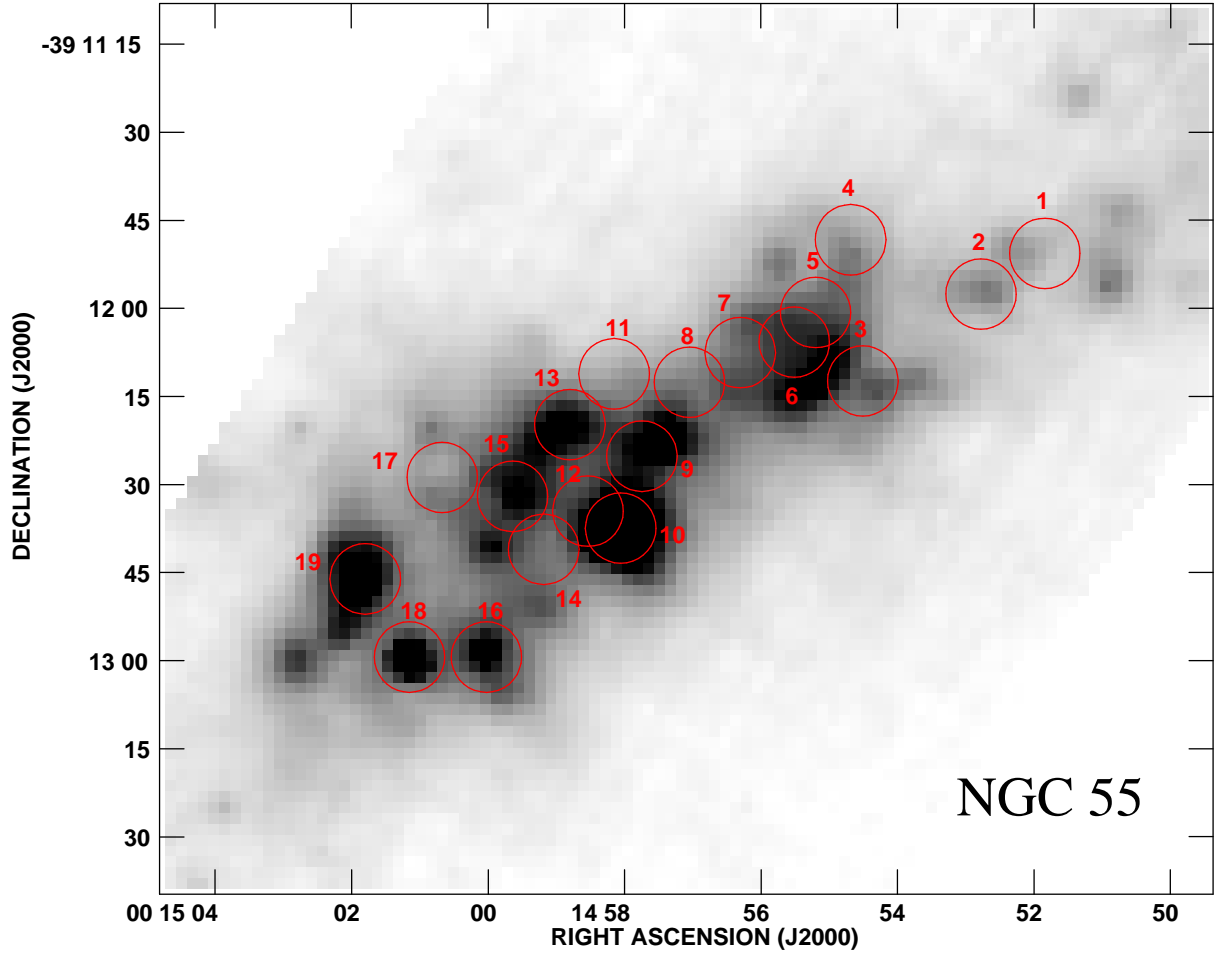


Fig. 13.— Full, integrated IRS map of NGC 55 with extraction regions labeled. Regions have a physical radius of 52.5 pc.

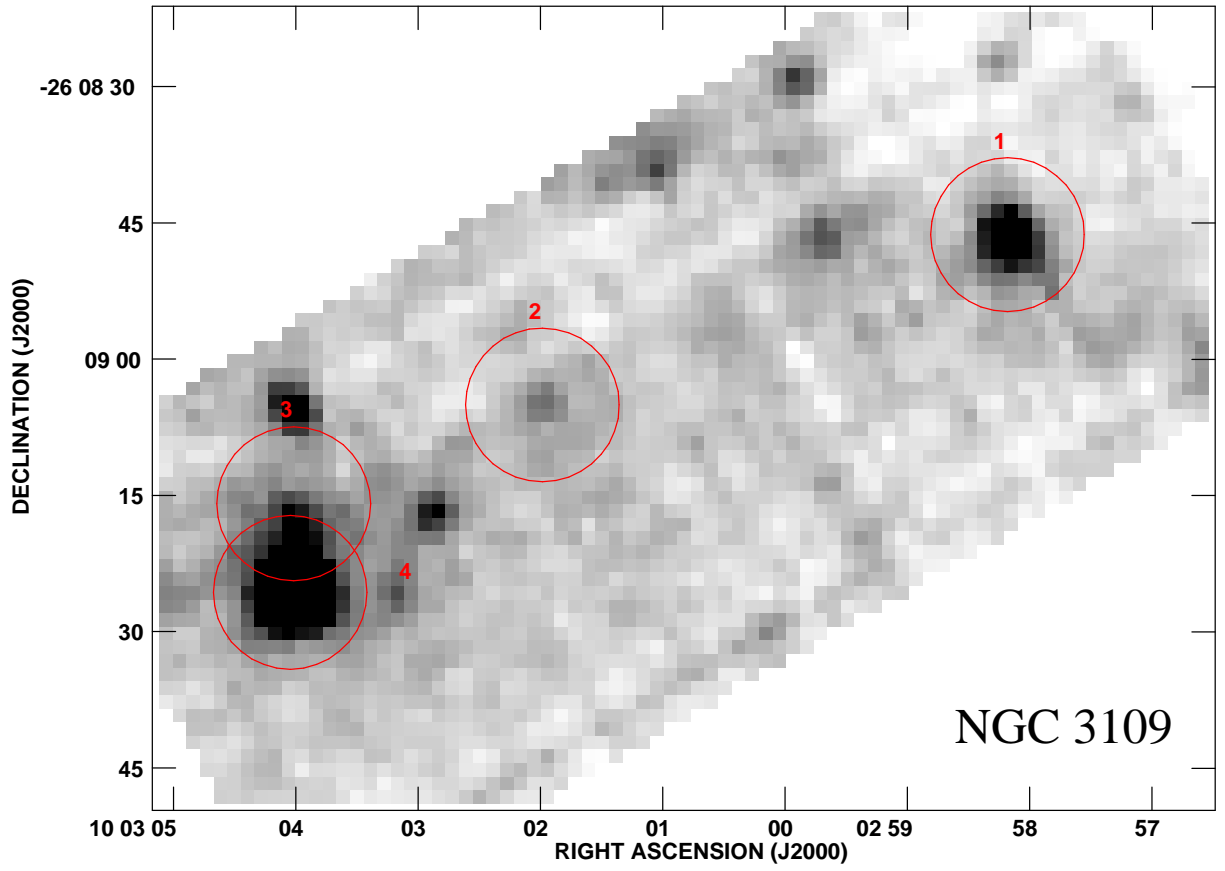


Fig. 14.— Full, integrated IRS maps of NGC 3109 with extraction regions labeled. Regions have a physical radius of 52.5 pc.

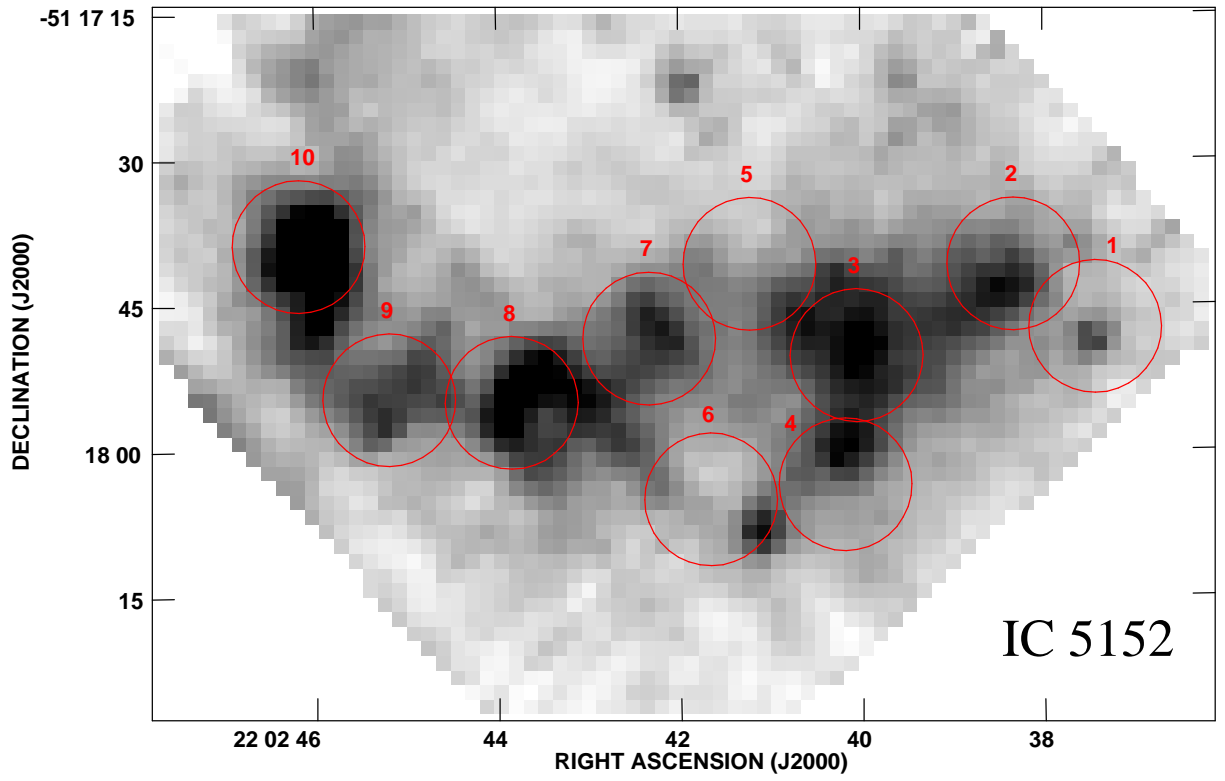


Fig. 15.— Full, integrated IRS map of IC 5152 with extraction regions labeled. Regions have a physical radius of 52.5 pc.

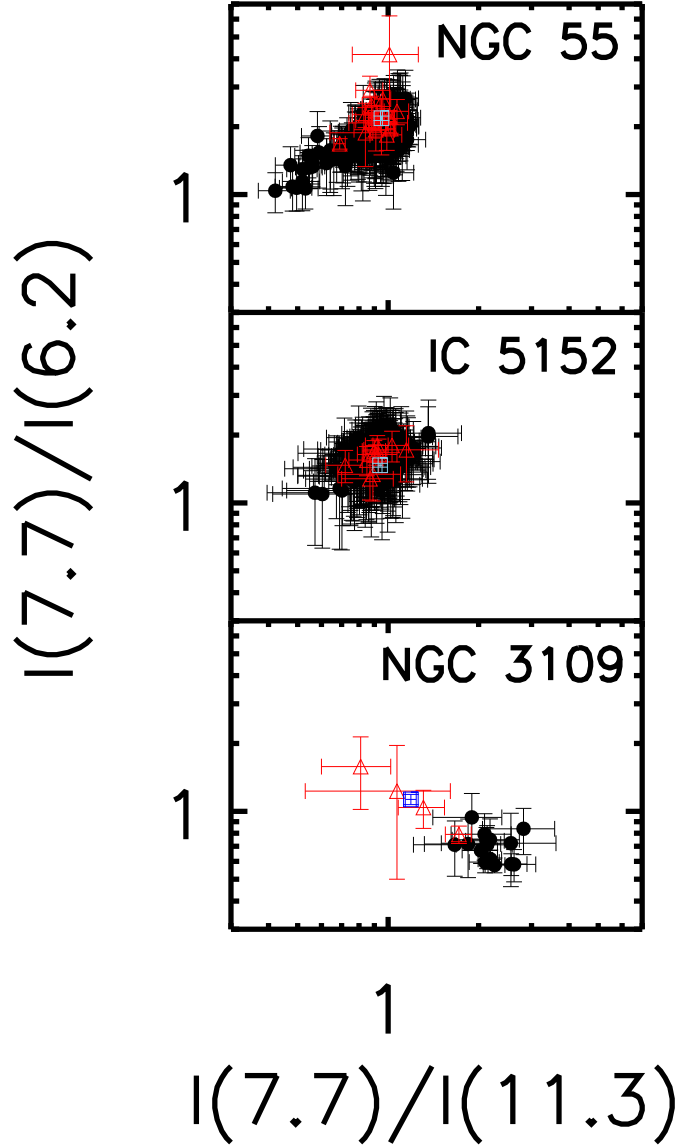


Fig. 16.— PAH radiance ratios within each galaxy. Pixel by pixel comparisons are shown in black, trimmed to show data above the 3σ level (note that in NGC 3109, which has generally low S/N, this causes an offset between the pixel cloud and the integrated regions, which include all pixels regardless of S/N level; see discussion in § 4). Points in red represent the integrated values from the 52.5 pc extracted regions. The blue point represents the global ratio.

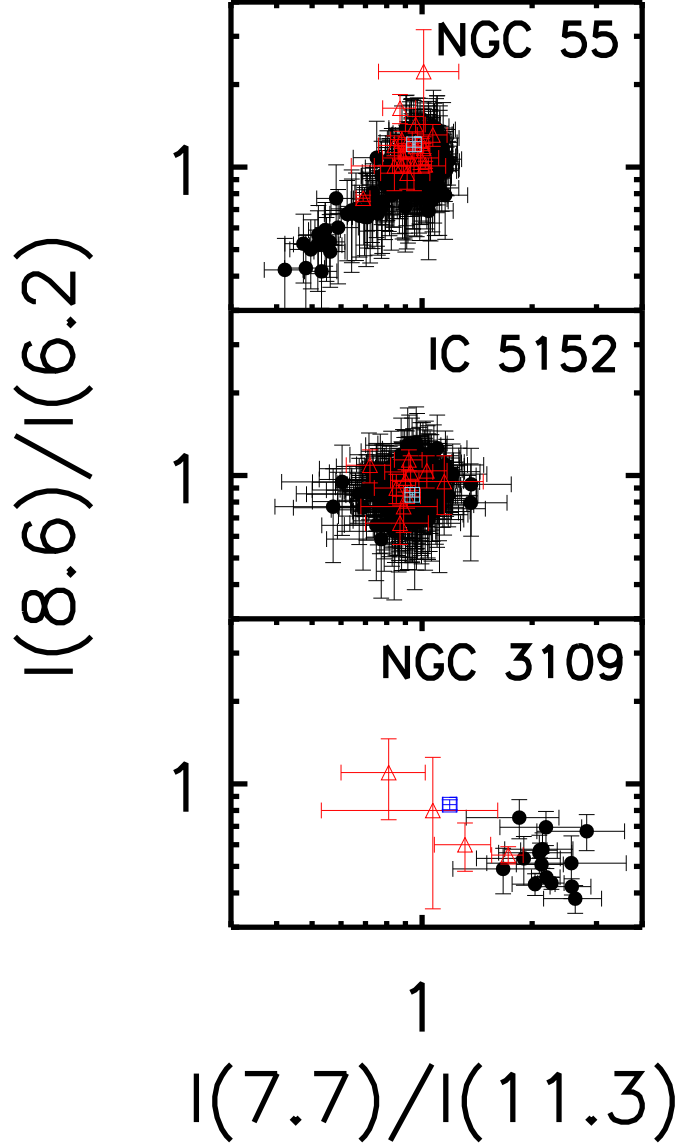


Fig. 17.— PAH radiance ratios within each galaxy. Pixel by pixel comparisons are shown in black, trimmed to show data above the 3σ level (note that in NGC 3109, which has generally low S/N, this causes an offset between the pixel cloud and the integrated regions, which include all pixels regardless of S/N level; see discussion in § 4). Points in red represent the integrated values from the 52.5 pc extracted regions. The blue point represents the global ratio.